The Thesis Committee for Alex James Pini
Certifies that this is the approved version of the following thesis:

Investigation of the Effect of Repeat Orbits on GRACE Gravity Recovery

APPROVED BY

SUPERVISING COMMITTEE:

Supervisor: ____
Srinivas Bettadpur

____
Byron Tapley

Investigation of the Effect of Repeat Orbits on GRACE Gravity Recovery

by

Alex James Pini, B.S.

THESIS

Presented to the Faculty of the Graduate School of
The University of Texas at Austin
in Partial Fulfillment
of the Requirements
for the Degree of

MASTER OF SCIENCE IN ENGINEERING

THE UNIVERSITY OF TEXAS AT AUSTIN
December 2012

Dedicated to the friends and family who have always been there for me.

Acknowledgments

First and foremost, I would like to thank my advisor and mentor Dr. Srinivas Bettadpur for his guidance and financial support over the past two years. His inquisitive nature and style of teaching is infectious, and this has been the most important gift he's given me as an engineer. He has continually challenged me to push myself and because of this I've grown in ways that I would never have imagined. Additionally, he listened to my research interests and provided me with work that was interesting and meaningful. His technical expertise is unparalleled, and many of my results have originated from his suggestions. Without him, this thesis would not exist.

I would like to thank Dr. Byron Tapley for the privilege to work at the Center for Space Research during my years as a graduate student. Working on a world-renowned satellite and being surrounded by those involved in its data analysis have undoubtedly resulted in a great learning experience. I'm extremely grateful for this unique opportunity. I would like to give special recognition to Dr. Steve Poole for teaching me the nuances of AESoP. There were many growing pains associated with learning this software, but his door was always open and he was very helpful when I needed to troubleshoot. His positive attitude and willingness to serve as a sounding board for my ideas greatly contributed to the progress of this thesis and will not soon be forgotten. I would also like to thank Dr. Himanshu Save and Dr. Peter Nagel for their contributions to the SVD work and generation of REGRES files associated with this thesis, respectively. They took time out of their days to field my questions and help me obtain results, and I appreciate their efforts. I would like to thank the Texas Advanced Computing Center for providing the supercomputers used to do much of the heavy lifting. Without access to their machines, I would not have a vast majority of these results.

Lastly, I would like to thank my parents for the various forms of support they have given me throughout my lifetime. Many of my greatest accomplishments thus far would simply not have been possible if not for their encouragement. Their advice and positive mentality have allowed me to stay focused and make it through my roughest patches. The can-do attitude and commitment to hard work that they possess have been instilled in me, and they've become an integral part of my development as an engineer. For 24 years they have pushed me to apply myself and reach for the stars, and now I can finally say I've achieved one of my biggest goals in life. I can't thank them enough.

Investigation of the Effect of Repeat Orbits on GRACE Gravity Recovery

by

Alex James Pini, M.S.E.
The University of Texas at Austin, 2012
SUPERVISOR: Srinivas Bettadpur

The Gravity Recovery and Climate Experiment (GRACE) has been orbiting the Earth and determining its gravity field since 2002. Throughout the course of the mission, the orbital elements occasionally change such that the satellites enter a repeat ground track configuration. Repeat ground tracks result in reduced spatial resolution of the satellites, which poses problems in the context of gravity recovery. The monthly gravity solutions during these periods are examined and shown to have lower quality than usual. The characteristics of these repeat period solutions are identified and compared to a period of uniform coverage to illustrate the ways in which the solutions are degraded. An investigation into the underlying physical and computational sources of these errors is also presented.

Table of Contents

List of Tables

List of Figures

Chapter 1

Introduction

1.1 Problem Statement

The Gravity Recovery and Climate Experiment (GRACE), a joint mission between NASA and Germany's DLR, consists of a pair of satellites that have been orbiting the Earth and collecting observations that result in monthly gravity field solutions since 2002. The mission principal investigator, science operations, and science data analysis responsibilities related to GRACE reside at the University of Texas at Austin's Center for Space Research. The orbit of GRACE (as with most geodetic satellites) is designed such that it passes over as much of the Earth's terrain as possible in a short amount of time. By doing this, GRACE experiences the gravitational effects of many different portions of the Earth and is therefore able to resolve them.

Throughout the course of the GRACE mission's lifetime, there have been a few periods of reduced spatial coverage, due to repeat ground tracks, resulting from the satellites' continually changing orbital elements. The repeat ground tracks cause GRACE to only observe a small fraction of the Earth's gravity field, and the gravity solutions using those observations suffer in terms of quality. The detrimental effects of repeat ground tracks on the "performance" of GRACE satellites has long been observed, and several techniques have been developed which improve the solution (such as matrix regularization and incorporation of an *a priori* constraint).

However, the fundamental reasons for why solutions during repeat ground tracks have reduced quality are still not fully understood. For GRACE, this thesis aims to identify some of the characteristics that are associated with solutions during repeat periods. In addition, the underlying causes of solution degradation from a physical and computational standpoint will be addressed.

1.2 History of Gravity Recovery

The determination of Earth's gravitational field has many important applications. As mentioned in Appendix A, the ability to effectively predict the motion of satellites relies heavily on an accurate model of the Earth's gravitational field. There is also an interest in the time-varying nature of the gravity field among climatologists [1]. The motion of the Earth's fluid envelope (oceans, atmosphere, and cryosphere) is observed as a change in mass distrubution, and scientists can use this information to study geophysical processes on a large scale [31].

Prior to the launch of Sputnik in 1957, the importance of determining the Earth's gravity field was recognized. However, the lack of data to support the field of geodesy's theory hindered its progress [23]. The gravitational field has traditionally been determined by empirically estimating its harmonic coefficients. The data from which these estimates are calculated comes from measurements taken from the surface of the Earth and by observing the non-spherical perturbing influence on the motion of satellites [8]. Before satellite tracking data became abundant, the most popular method of determining the Earth's gravitational field was to analyze the amplified long-period behavior of satellites in resonant orbits [6]. One of the first demonstrations of this technique involved observing the sinusoidal varition in the orbital eccentricity of the Vanguard satellite 1958β_2 [16]. The amplitude and period of the variation provided information about the source and size of the dominant perturbation responsible for that effect, which was found to be the J_3 zonal harmonic.

The earliest attempts to recover the harmonic coefficients were founded upon analytical theories of satellite motion, such as linear perturbation theory [10]. However, with the advent of more powerful computers and better observation technology, numerical approaches emerged that were capable of determining higher fidelity gravity fields [23].

The first release of a gravity model came in 1963 from the Johns Hopkins University/Applied Physics Laboratory. It was labeled JHU/APL 1.0 and contained harmonic coefficient values up to degree and order eight [28]. Other ways to refer to the size of a gravity field include saying that it has $L_{MAX} = 8$ or calling it an 8×8 field. Various other models were created by different institutions with slightly increasing size over the next ten years, and in 1972 NASA Goddard Space Flight Center generated the first in its line of Goddard Earth Models (GEM) [22]. The GEM series incorporated additional data types to resolve the gravity fields, such as satellite radar altimetry, Doppler range observations, and satellite laser ranging [8]. The GEM models featured successive improvements, culminating in the GEM-T3 model in 1992 that was complete to degree and order 50. The GEM series was followed in the mid 1990's by the Joint Gravity Model series (JGM-1, 2, and 3) that included harmonic coefficients up to degree and order 70 [14]. The University of Texas at Austin independently created its own Texas Earth Gravity (TEG) models from the late 1980's to late 1990's. In 1997, the TEG-3 model was released and was complete to degree and order 70. It was also the first model to include GPS observations (associated with the TOPEX/Poseidon mission) in the gravity solution process [22]. These models ultimately resulted in the widespread EGM96 gravity field.

The success of TOPEX/Poseidon demonstrated the value of GPS measurements in orbit determination and gravity recovery, and this technique has been included in the major subsequent geodetic missions to date. These missions include GRACE, the Challenging Minisatellite Payload (CHAMP, launched in 2000), and the Gravity Field and Steady-State Ocean Circulation Explorer (GOCE, launched in 2009). In addition to obtaining precise position data, these three missions have instruments on board to measure non-gravitational accelerations so that they could be separated from the influence of the Earth's gravity. The GRACE mission's instrument suite includes a high-precision K-band ranging system, causing a paradigm shift in the way the Earth's gravity field is measured.

1.3 GRACE Mission Design

The GRACE mission consists of two co-orbiting satellites in a nearly circular orbit around the Earth. The near-circular orbit is a common choice among geodetic satellites because it allows for a "uniform" gravitational influence from the Earth [13]. The satellites' orbits are also nearly polar ($\sim 89^\circ$ inclination) to allow for maximum spatial coverage of the Earth's surface with little to no additional maneuvering. Ideally, a geodetic satellite should be placed in an orbit with the lowest possible altitude because the gravity signal is attenuated as the semi-major axis increases. However, the drag experienced from Earth's atmosphere will quickly decay the orbit of a low-altitude satellite, so a compromise must be made between the signal quality, the fuel consumption, and the lifetime of the mission. GRACE was chosen to have a relatively high altitude (~ 500 km) and was allowed to free-fall with few corrective maneuvers. At this height, the satellites' altitudes decay at only about 30 m/day [24]. This technique was selected in order to obtain a longer mission lifetime. By doing this, the time-variable gravity field of the Earth could be observed for longer durations, which is beneficial for climatological applications [1].

As with the CHAMP mission that preceded it, GRACE incorporates GPS measurements to precisely determine its orbits and three-axis accelerometers to measure the non-gravitational forces it encounters. However, the advantage of using two satellites in this configuration is that inter-satellite range measurements (also known as low-low satellite to satellite tracking) observe the nonspherical gravitational perturbations associated with the Earth with greater precision. The high precision of the K-Band antenna ranging system (< 10 μm [9]) has allowed for the range measurements to become the primary observation of the GRACE mission. The sensitivity achieved with the inter-satellite measurement system enables smaller orbital perturbations at higher frequencies to be accurately resolved [1]. The resulting gravity fields that are generated using GRACE data are complete to degree and order 180.

1.4 Thesis Scope and Approach

Throughout the lifetime of the GRACE mission, there has nearly always been a sufficient amount of data to produce these high-fidelity monthly gravity solutions with great accuracy. However, as mentioned previously, the geometries of the satellites' orbits are such that certain periods will contain less information about the Earth's gravity field than usual. The gravity solutions that are obtained from this reduced data set suffer in terms of quality in that there is increased uncertainty in the estimated harmonic coefficients. The investigation of the underlying reasons for why this degradation occurs is the central focus of this thesis.

Several techniques and performance metrics will be examined in this thesis to identify and characterize the nature of gravity solutions during months of reduced spatial coverage. This will be done using both real and simulated scenarios that highlight the important details associated with solution degradation. The concept of gravitational perturbation frequencies will be discussed, as well as their behavior during repeat ground tracks. The relationship between these perturbation frequencies and the mathematical conditioning of the estimation problem used to estimate Earth's harmonic coefficients is also addressed. In addition, analytic tools such as the singular value decomposition and degree error variance comparisons will be utilized to observe the onset of solution degradation and why it happens from a computational standpoint. Additionally, to assess the practicality of the results obtained from this analysis, certain quantities will be compared to more widely used calibrated solutions. First, the theory behind these fundamental concepts will be presented.

Chapter 2

Theory

The sections contained within this chapter focus on the topics that are directly related to the problems associated with gravity recovery during repeat ground tracks. For a more rigorous description of the fundamentals of geodesy, the techniques used to produce gravity solutions, and the associated terminology, refer to the appendices at the end of this thesis.

The underlying goal of the GRACE mission is to observe and determine the properties of Earth's gravity field, particularly its non-spherical contribution. An accurate representation of the Earth's influence on a satellite is essential to predicting its motion at a future time. This relationship is shown by the expression for the acceleration of a satellite due to gravity:

$$\ddot{\boldsymbol{r}} = \nabla U \tag{2.1}$$

where ∇ denotes the gradient of the scalar potential function U and $\ddot{\boldsymbol{r}}$ is a vector containing the three components of the satellite's acceleration. For the remainder of this thesis, bold symbols will denote vector and matrix quantities to distinguish them from scalars. It can be seen from Equation 2.1 that the calculated acceleration on the satellite is dependent on the value of U. The potential function is often decomposed into effects from the spherical portion of the body, which is known to be $\frac{\mu}{r}$, and the non-spherical influences on the satellite that cause deviations from ideal Keplerian motion, known as perturbations. Assuming that the only perturbations acting on the satellite are due to the non-spherical contributions of Earth's gravity, the accuracy of the spherical hamonic coefficients of the Earth become the determining factor for the quality of the predicted motion.

The nonspherical gravitational potential experienced by a satellite is dependent on its position with respect to the Earth. A convenient way of expressing the location of a satellite in this regard is to employ a spherical coordinate system of geocentric latitude ϕ, longitude λ, and radius r from the Earth's center of mass. With this convention in place, the nonspherical gravitational influence can be shown to be:

$$U_{NS} = \frac{\mu}{r} \sum_{l=2}^{\infty} \sum_{m=0}^{l} \left(\frac{a_e}{r} \right)^l \overline{P}_{lm} (\sin \phi) \left[\overline{C}_{lm} \cos (m\lambda) + \overline{S}_{lm} \sin (m\lambda) \right] \tag{2.2}$$

where a_e represents the Earth's equatorial radius and $\overline{P}_{lm}$ is the normalized associated Legendre function evaluated for degree l and order m of the expansion. Additionally, these perturbations can be visualized in terms of the Keplerian elements associated with the the satellite's orbit using Kaula's linearized perturbation theory [10]. The potential function of interest becomes:

$$U_{NS} = \sum_{l=2}^{\infty} \sum_{m=0}^{l} \sum_{p=0}^{l} \sum_{q=-\infty}^{+\infty} \frac{\mu}{a} \left(\frac{a_e}{a}\right)^l F_{lmp}\left(i\right) G_{lpq}\left(e\right) S_{lmpq} \tag{2.3}$$

where a is the semi-major axis and F_{lmp} and G_{lpq} are functions of the inclination i and eccentricity e of the orbit. As in Equation 2.2, the parameters l and m correspond to the degree and order of the various harmonic coefficients of the Earth. The term S_{lmpq} is represented by:

$$S_{lmpq} = \begin{bmatrix} C_{lm} \\ -S_{lm} \end{bmatrix} \cos\psi_{lmpq} + \begin{bmatrix} S_{lm} \\ C_{lm} \end{bmatrix} \sin\psi_{lmpq} \tag{2.4}$$

where the upper term in the brackets is used when $l - m$ is even and the lower term is used when $l - m$ is odd. Also, the angular term, which is sometimes referred to as the Kaula gravitational argument [27] is:

$$\psi_{lmpq} = (l - 2p + q)M + (l - 2p)\omega + m(\Omega - \theta_e) \tag{2.5}$$

where ω, M, and Ω are the classical Keplerian elements and θ_e is the Greenwich hour angle [1].

2.1 Non-Spherical Body Perturbation Frequencies

The rate at which ψ_{lmpq} is changing is known as the gravitational perturbation frequency. The perturbation frequency is obtained by simply taking the time derivative of Equation 2.5:

$$\dot{\psi}_{lmpq} = (l - 2p + q)\dot{M} + (l - 2p)\dot{\omega} + m(\dot{\Omega} - \dot{\theta}_e) \tag{2.6}$$

Perturbation frequencies play an important role in geodesy and gravity recovery because they are linked to the period of oscillation for a particular perturbation. Different harmonic coefficients are associated with different $lmpq$ sets, resulting in different perturbation frequencies. These frequencies dictate the behavioral characteristics of the perturbing source, such as whether they exhibit secular, long period, or short period effects. An alternate form of $\dot{\psi}_{lmpq}$ will be used for the remainder of this thesis:

$$\dot{\psi}_{kmq} = -q\dot{\omega} + k(\dot{\omega} + \dot{M}) + m(\dot{\Omega} - \dot{\theta}_e) \tag{2.7}$$

where $-l \leq k \leq l$. The coefficient $k = l - 2p + q$ is introduced for convenience to identify lumped harmonic sets, which will be discussed shortly. The index q contributes to the eccentricity function $G_{lpq}(e)$ associated with Kaula's formulation of the gravitational potential listed in Equation 2.3 [10]. Noting that $G_{lpq} \sim e^{|q|}$, a nearly-circular orbit, as seen with the GRACE mission, causes perturbations associated with $q = 0$ to have the dominant effects. Because of this, perturbations with nonzero q values, sometimes referred to as sideband frequencies [6], will not be considered in this thesis. Under these conditions, the general form for the dominant perturbation frequencies for a given orbit is:

$$\dot{\psi}_{km0} = k(\dot{\omega} + \dot{M}) + m(\dot{\Omega} - \dot{\theta}_e) \tag{2.8}$$

It can be seen that for a specified orbit, each m, k pair will almost always produce a unique perturbation frequency. Considering that multiple combinations of l and p can produce the same value of k, each perturbation frequency can be attributed to a linear combination of many different harmonic coefficients. More specifically, these coefficients will share the same m, but the nature of k dictates that each degree l in the set will have the same mathematical parity. As a result, each m, k pair corresponds to a set of lumped harmonics [5]. In other words, when perturbations of a particular frequency are observed, many different harmonic coefficients are responsible.

The concept of lumped harmonics can be demonstrated with a simple example involving a small gravity field. Consider the GRACE mission, which at a particular moment has the following orbital properties:

$$\begin{aligned}
\dot{\omega} &= -4^\circ/day \\
\dot{\Omega} &= -0.1^\circ/day \\
\dot{M} &= 5504^\circ/day \\
\dot{\theta}_e &= 360^\circ/day
\end{aligned}$$

The perturbation frequencies corresponding to each pair ($\overline{C}_{lm}$, $\overline{S}_{lm}$) of harmonic coefficients in a 7×7 field are calculated via Equation 2.6. By grouping the coefficients that have identical frequencies, some relationships between the indices of the coefficients become apparent. To illustrate this, the lowest positive frequencies for the test field are listed and organized below:

Table 2.1: Perturbation Frequencies Produced by Different Harmonic Coefficients

Freq. (*cycles*/*rev*)	l	p	m	k
0.00	2	1	0	0
0.00	4	2	0	0
0.00	6	3	0	0
0.52	7	3	7	1
0.58	7	3	6	1
0.64	5	2	5	1
0.64	7	3	5	1
0.70	5	2	4	1
0.70	7	3	4	1
0.77	3	1	3	1
0.77	5	2	3	1
0.77	7	3	3	1
0.83	3	1	2	1
0.83	5	2	2	1
0.83	7	3	2	1
0.89	3	1	1	1
0.89	5	2	1	1
0.89	7	3	1	1
0.95	3	1	0	1
0.95	5	2	0	1
0.95	7	3	0	1
1.53	6	2	6	2
1.60	6	2	5	2
1.66	4	1	4	2
1.66	6	2	4	2
⋮	⋮	⋮	⋮	⋮

The results in Table 2.1 show that coefficients with the same perturbation frequency have the same values of m and k. Furthermore, these groups of coefficients share the same parity of l, meaning that the values of l are either entirely even or odd. While the existence of multiple harmonic coefficients contributing to a single perturbation frequency makes it difficult to observe the effects of a single coefficient, techniques have been established for decades to estimate the coefficients with considerable accuracy [11],[12]. When this is the case, considerations have to be made regarding sampling frequency and measurement duration to ensure observability.

A special case involving perturbation frequencies is known as resonance. This occurs when a particular ψ_{kmq} (excluding those that correspond to even-degree zonal harmonics) changes very slowly, such that $\dot{\psi}_{kmq} \approx 0$ [5]. A satellite is said to be in exact resonance when $\dot{\psi}_{kmq} = 0$, but this is a very rare occurrence. In reality, the most extreme scenarios exist when the magnitude of $\dot{\psi}_{kmq}$ is very small (known as deep resonance), which means the perturbation frequency is very low and the oscillations take place over a very long period. Since perturbations with longer periods are known to have larger amplitudes [27], the lumped harmonic sets responsible for this behavior will dominate the signal and other harmonics will become less resolvable. Another category with slightly larger $\dot{\psi}_{kmq}$ than deep resonance is shallow resonance, which has less profound effects but still poses problems in the context of gravity field recovery. A common example of an orbital configuration that exhibits resonance is the repeat ground track.

2.2 Repeat Ground Tracks

As mentioned in Chapter 1, geodetic missions such as GRACE are often chosen to have near-polar inclinations as a fuel-efficient technique to provide maximum spatial coverage. A quick way to assess the "resolution" achieved by a satellite is by analyzing the ground track, or the projection of the satellite's orbit onto the surface of the Earth, over a reasonably short interval of time. Ideally, the ground track of a satellite will uniformally cover the Earth in this span so that the perturbing effects of a wide range of spherical harmonics can be observed. However, conditions can occasionally arise such that the satellite exhibits a repeat ground track, upon which the ground track only covers a relatively small portion of the Earth. Examples of these two scenarios are shown in Figure 2.1 below for two month-long intervals during the GRACE mission.

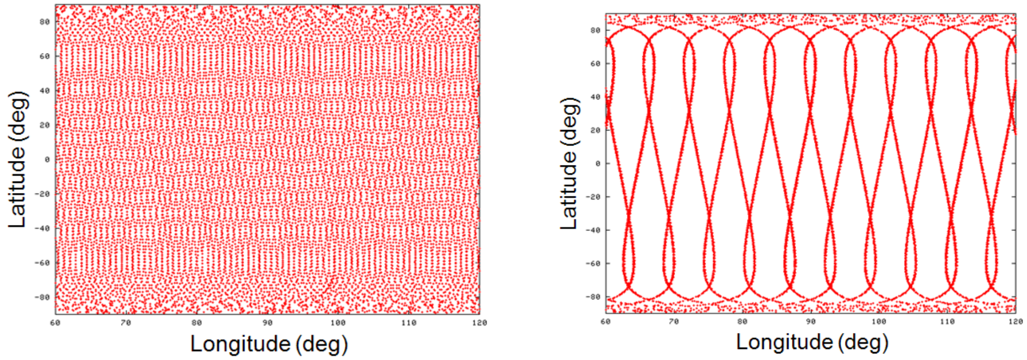

(a) February 2004

(b) September 2004

Figure 2.1: Ground track layout during a period of (a) ideal spacing and (b) repeat ground track conditions.

Figure 2.1a illustrates the desirable spatial coverage for a geodetic satellite, occurring during the month of February 2004. A vast majority of the months in the GRACE mission's lifetime possess a ground track layout similar to this, but occasionally the orbital elements combine to produce a repeat ground track such as in Figure 2.1b. This particular repeat period occurred during September 2004 and is widely-studied because it represents the "worst" case of a repeat period that GRACE has encountered. The large portions of uncovered terrain are clearly visible in this plot, which will later be shown to have an adverse effect on the ability to recover the Earth's gravity field.

Repeat ground tracks occur when the rotational period of the Earth and the orbital period of the satellite are commensurate, meaning their ratio is comprised of two co-prime integers [27]. These two entities are mathematically represented by the nodal day and nodal period, respectively. The nodal day is defined as the time required for the Earth to make one revolution relative to the satellite's line of nodes [25]:

$$D_n = \frac{2\pi}{\dot{\theta}_e - \dot{\Omega}} \tag{2.9}$$

Similarly, the nodal period is defined as the amount of time it takes for a satellite to cross from ascending node to ascending node:

$$P_n = \frac{2\pi}{\dot{\omega} + \dot{M}} \tag{2.10}$$

When the nodal period of the satellite and the nodal day are in proportion to each other, a repeat ground track is encountered. That is, the following equations hold true for exact repeat ground tracks [19]:

$$\begin{aligned} D\frac{2\pi}{\dot{\theta}_e - \dot{\Omega}} &= R\frac{2\pi}{\dot{M} + \dot{\omega}} \\ \frac{R}{D} &= \frac{\dot{M} + \dot{\omega}}{\dot{\theta}_e - \dot{\Omega}} \end{aligned} \tag{2.11}$$

where D and R are co-prime integers which denote the length of the repeat period in days and number of orbital revolutions that the satellite makes in that time, respectively. Theoretically, all orbits will repeat if given enough time and revolutions, but only small values of D and R produce the sparse ground tracks of interest. For example, the repeat ground track that GRACE experienced in September 2004 was 61 revolutions over 4 days (referred to as 61/4).

2.2.1 Behavior of Perturbation Frequencies During Repeat Ground Tracks

During exact repeat conditions, the relationship between the changes in orbital elements is such that multiple perturbation frequencies reduce to a unique frequency over the same period [30]. The spectrum of unique frequencies becomes altered in a manner similar to aliasing. This effect can be visualized by substituting the repeat ground track condition into the expression for the general perturbation frequency (Equation 2.8):

$$
\begin{aligned}
\dot{\Omega} - \dot{\theta}_e &= -\frac{D(\dot{M} + \dot{\omega})}{R} \\
\dot{\psi}_{km0} &= k(\dot{M} + \dot{\omega}) + m\left[-\frac{D(\dot{M} + \dot{\omega})}{R}\right] \\
&= (kR - mD)\frac{(\dot{M} + \dot{\omega})}{R} \\
&= N\frac{(\dot{M} + \dot{\omega})}{R} \qquad (2.12)
\end{aligned}
$$

where $N = kR - mD$ is known as the wave number for a given repeat period of D days [30]. Since $\frac{(\dot{M}+\dot{\omega})}{R}$ is essentially constant during the repeat ground track portion of any orbit, the wave number becomes an alternate way to characterize perturbation frequencies. Considering that positive and negative perturbation frequencies with the same magnitude can be lumped together, there will be $|N|$ unique frequencies associated with a satellite in a repeating ground track. Depending on the size of the gravity field that is to be determined, there could potentially be some identical frequencies in the repeat configuration that were originally distinct in the general case.

2.2.2 Consequences of Repeat Perturbation Frequencies

In the event of this scenario, the resulting solution for Earth's gravity field will most likely be of lower quality than usual. This consequence can be traced back to the estimation problem that is used to determine the harmonic coefficients that make up the gravity field. The numerical conditioning of this problem is dependent on the ratio of the number of unique perturbation frequencies to unknown harmonic coefficients to be solved for. When the gravity field to be determined becomes large enough, the reduction in unique perturbation frequencies experienced during a repeat ground track will adversely affect the observability of the estimation problem. This phenomenon will be discussed in detail in Chapter 4.

When GRACE encounters a repeat ground track, a threshold is reached at which the size of a gravity field is too large (that is, it contains too many harmonic coefficients) to be adequately resolved. Considering that the number of coefficients steadily rises with the size of the field, the first signs of degradation become apparent when perturbation frequencies start to repeat that were previously unique in a non-repeat ground track. Ultimately, the requirement to guarantee the same number of perturbation frequencies between uniform and sparse ground track layouts is that $R > 2L_{MAX}$. When this condition, which is sometimes referred to as the Colombo-Nyquist rule [29], is no longer fulfilled, the estimation problem becomes less observable.

There are several tools for comparing gravity solutions such that the effects of a lack of information can be identified. These tools are detailed in the following section.

2.3 Analysis Tools for Gravity Field Solutions

The analysis tools that are used in this thesis to assess the quality of a gravity field solution can be divided into two categories. The first group looks at the values of the estimated coefficients and the size of their uncertainties.

These metrics are a relatively high-level look at the statistics of a gravity field solution and can be used to quickly compare different fields. The second technique, which is the singular value decomposition, provides a more in-depth look into the numerical conditioning of the estimation problem used to obtain the solution. The singular value decomposition helps to identify when and why a solution is degraded under certain conditions.

2.3.1 Degree Variance, Degree Difference Variance, and Degree Error Variance

The degree variance, degree difference variance, and degree error variance are three closely related statistics that are used to assess the quality of a gravity solution. These statistics are commonly plotted with the degree l of the field along the abscissa so that the contribution of particular coefficients in the spectrum can be identified. For example, the degree variance (DV) is calculated via:

$$\sigma_{l_{DV}} = \sqrt{\sum_{m=0}^{l} \left[\overline{C}_{lm}^{2} + \overline{S}_{lm}^{2}\right]} \tag{2.13}$$

The degree variance is a measure of the signal "power" associated with a particular gravity field in that it directly involves the values of the normalized harmonic coefficients. As a result, examining the DV spectrum is done as a quick check to ensure that a candidate field is comparable to an accepted power law [18]. In the absence of a nominal field, a baseline can be approximated by Kaula's Rule [17], which is a best-fit curve that is derived from empirical measurements of Earth's gravity field throughout history:

$$\sigma_{l_{DV}} \approx 10^{-5}\frac{\sqrt{2l+1}}{l^2} \tag{2.14}$$

While a visual inspection of the DV for two different fields serves as a useful method for comparison, a more quantitative approach is sometimes desired. This is achieved by calculating the degree difference variance (DDV). First, the difference between the values of each harmonic coefficient for the two fields is obtained ($\Delta\overline{C}_{lm}$ and $\Delta\overline{S}_{lm}$). Then, the sum of the squares is computed for each coefficient within a particular degree in the same manner as the degree variance:

$$\sigma_{l_{DDV}} = \sqrt{\sum_{m=0}^{l}\left[(\Delta\overline{C}_{lm})^2 + (\Delta\overline{S}_{lm})^2\right]} \tag{2.15}$$

The DV and DDV are good tools to compare two gravity fields, but contain little information about the estimation uncertainty associated with the estimates for the harmonic coefficients. The degree error variance (DEV) is used to help visualize the amount of uncertainty that is contributed by the coefficients in each degree [8]. The DEV is calculated by taking the sum of the squares of the formal sigmas (the diagonals of the covariance matrix) of all coefficients for a given degree:

$$\sigma_{l_{DEV}} = \sqrt{\sum_{m=0}^{l}\left[\sigma^2_{\overline{C}_{lm}} + \sigma^2_{\overline{S}_{lm}}\right]} \tag{2.16}$$

The three formulations above result in dimensionless statistics, but they are more commonly represented in units of geoid height. This is achieved by multiplying the dimensionless value by the mean equatorial radius of the Earth.

As mentioned previously, the DEV uses the formal sigmas associated with the estimation problem to establish a measure of a gravity field's uncertainty. Although the aforementioned formal degree error variances will be used in this thesis, a more realistic set of calibrated error estimates is also delivered to the scientific community [2]. The calibrated errors used for this analysis are modified versions of those that are contained within the GRACE Release 4 (RL04) product. The RL04 values are divided by a factor of $\sqrt{2}$ in order to roughly represent the errors that will be seen as part of the transition by the GRACE science team to RL05, which includes many improvements upon the previous release. The RL05 calibrated errors were not available at the time of writing this thesis.

Calibrated errors are useful because they account for systematic flaws, such as an assumption of Gaussian noise in the instrument measurements, and tend to be more conservative in that they have higher uncertainties. The calibrated error estimates are essentially used to replace the formal sigmas, so the degree error variance of these new sigmas can also be calculated using Equation 2.16. While the calibrated solutions are are considered to be more realistic, the formal sigmas arising from "typical" GRACE data processing are analyzed because they are generated relatively quickly. Regardless, the calibrated error DEV serves as a good baseline to assess how significant the relative changes in formal DEV's are between gravity solutions. This topic will be addressed further in Chapter 4.

2.3.2 Singular Value Decomposition of the $\boldsymbol{R}$ Matrix

The singular value decomposition (SVD) is a powerful and prevalent tool used to manipulate a rank-deficient linear system such that it enables a meaningful solution to be resolved. A by-product of this process is the ability to determine the observability of a system by inspecting the singular values associated with it [8]. The use of techniques will be explained in further detail, but first the fundamentals behind the SVD will be established.

Given any $m \times n$ matrix $\boldsymbol{A}$, there exists a set of three matrices that form the singular value decomposition of $\boldsymbol{A}$, such that:

$$\boldsymbol{A} = \boldsymbol{U}\boldsymbol{\Sigma}\boldsymbol{V}^T \tag{2.17}$$

where $\boldsymbol{U}$ and $\boldsymbol{V}$ are orthogonal matrices. They are composed of column vectors $\boldsymbol{u}_i$ and $\boldsymbol{v}_i$ known as the ith left and right singular vectors, respectively [8]. Furthermore, $\boldsymbol{\Sigma}$ is a diagonal matrix that is $n \times n$ for traditional gravity recovery problems, where the number of m observations greatly outnumber the number of n parameters. The diagonal values of $\boldsymbol{\Sigma}$ are known as the singular values associated with $\boldsymbol{A}$. The singular values are commonly listed in descending order and are always greater than or equal to zero, such that $\sigma_1 \geq \sigma_2 \geq \ldots \geq \sigma_n \geq 0$. The analysis in this thesis adheres to this convention.

Knowledge of the singular values is useful because the number of nonzero singular values is equivalent to the rank of $\boldsymbol{A}$. Therefore, the extent to which a system is ill-conditioned can be determined by inspecting the singular values associated with it. In practical applications, however, ill-conditioned problems will never be exactly rank deficient, but rather numerically rank deficient [22]. This corresponds to the appearance of singular values that are very small, but not quite zero.

Techniques have been devised to identify the "bad" singular values in a problem, discard them, and reconstruct the problem using the singular vectors so that a pseudo-inversion can be performed as a meaningful alternative [8]. In essence, this procedure attempts to extract the linearly independent information and form a similar problem that is well-conditioned [22]. Considerable work has been done to determine which singular values are candidates for removal, and several criteria exist to determine the optimal solution for a given problem. This process of reconstructing the problem is outside the scope of this thesis, but the inspection of singular values to identify observability issues plays a major role in the subsequent analysis.

The term "ill-conditioned" generally refers to a system of linear equations that does not contain enough information to adequately determine the parameters of interest. Because the singular values of a system are closely linked to its conditioning, there are two categories of ill-conditioned problems that are determined by the characteristics of the singular value set [22]. The first class contains situations that have a distinct separation between large and small singular values and are referred to as rank deficient problems. The second class, known as discrete ill-posed problems, have a smooth transition from large to small singular values and are more commonly seen in applications related to gravity recovery. Although the smallest singular values might not be particularly close to zero, the overall range of values can be large enough to lead to numerical problems in certain situations. To demonstrate this, consider a basic linear system:

$$\boldsymbol{A}\boldsymbol{x} = \boldsymbol{b} \tag{2.18}$$

where $\boldsymbol{A}$ is a matrix and $\boldsymbol{x}$ and $\boldsymbol{b}$ are vectors. If $\boldsymbol{A}$ is full-rank, then the solution to the linear system is simply:

$$\boldsymbol{x} = \boldsymbol{A}^{-1}\boldsymbol{b} \tag{2.19}$$

If a small perturbation $\delta\boldsymbol{b}$ is added to $\boldsymbol{b}$, creating a new value $\tilde{\boldsymbol{b}}$, then it is desired that the new solution (denoted $\tilde{\boldsymbol{x}}$) should generally not be too far away from $\boldsymbol{x}$. The difference in the original and perturbed solutions will also be small, and is introduced as $\delta\boldsymbol{x} = \tilde{\boldsymbol{x}} - \boldsymbol{x}$. In this context, a perturbation is considered to be small when the norm of the perturbed vector is small relative to the norm of the original vector. In other words, the perturbations $\delta\boldsymbol{b}$ and $\delta\boldsymbol{x}$ are sufficiently small when the ratios $\frac{||\delta\boldsymbol{b}||}{||\boldsymbol{b}||}$ and $\frac{||\delta\boldsymbol{x}||}{||\boldsymbol{x}||}$ are small. With these relationships in place, the perturbed linear system becomes:

$$\begin{aligned} \boldsymbol{A}\tilde{\boldsymbol{x}} &= \tilde{\boldsymbol{b}} \\ \boldsymbol{A}(\boldsymbol{x} + \delta\boldsymbol{x}) &= \boldsymbol{b} + \delta\boldsymbol{b} \end{aligned} \tag{2.20}$$

Since the original linear system is defined to be $\boldsymbol{A}\boldsymbol{x} = \boldsymbol{b}$, the resulting expression is then:

$$\begin{aligned} \boldsymbol{A}\delta\boldsymbol{x} &= \delta\boldsymbol{b} \\ \delta\boldsymbol{x} &= \boldsymbol{A}^{-1}\delta\boldsymbol{b} \end{aligned} \tag{2.21}$$

Because the inversion of $\boldsymbol{A}$ is necessary, it is assumed to be full rank. Taking the induced matrix norm of Equation 2.21 results in the following inequality:

$$||\delta\boldsymbol{x}|| \leq \left|\left|\boldsymbol{A}^{-1}\right|\right| \, ||\delta\boldsymbol{b}|| \tag{2.22}$$

Similarly, the equation for the original linear system can be re-written as $\boldsymbol{b} = \boldsymbol{A}\boldsymbol{x}$. The induced matrix norm of this expression leads to:

$$||\boldsymbol{b}|| \leq ||\boldsymbol{A}|| \, ||\boldsymbol{x}|| \tag{2.23}$$

The norms $||\boldsymbol{b}||$ and $||\boldsymbol{x}||$ are scalar quantities, so they can be rearranged to form:

$$\frac{1}{||\boldsymbol{x}||} \leq ||\boldsymbol{A}|| \, \frac{1}{||\boldsymbol{b}||} \tag{2.24}$$

The perturbed and unperturbed inequalities can now be multiplied together to obtain a relationship between the relative sizes of the perturbation in $\boldsymbol{b}$ and the perturbation in $\boldsymbol{x}$:

$$\frac{||\delta \boldsymbol{x}||}{||\boldsymbol{x}||} \leq ||\boldsymbol{A}|| \, \left|\left|\boldsymbol{A}^{-1}\right|\right| \, \frac{||\delta \boldsymbol{b}||}{||\boldsymbol{b}||} \tag{2.25}$$

Equation 2.25 establishes the maximum value of the perturbed solution for a given perturbation in $\boldsymbol{b}$. This relationship is heavily dependent on the characteristics of $\boldsymbol{A}$, particularly on the value of the condition number κ [4]:

$$\begin{aligned} \kappa &= ||\boldsymbol{A}|| \, \left|\left|\boldsymbol{A}^{-1}\right|\right| \\ &= \frac{\sigma_1(\boldsymbol{A})}{\sigma_n(\boldsymbol{A})} \end{aligned} \tag{2.26}$$

where σ_1 and σ_n are the largest and smallest singular values of $\boldsymbol{A}$, respectively. In a well-conditioned problem, a small change in $\boldsymbol{b}$ will not affect the resulting solution very much, which corresponds to a small condition number. On the other hand, ill-conditioned problems can experience very large changes to the solution in the presence of a perturbation, so their condition numbers will be relatively high. As a result, the condition number becomes a measure of the "sensitivity" of a linear system. In other words, the size of the condition number can be used to assess how ill-conditioned a particular problem is.

This diagnostic technique can be applied to the QR factorization method used in GRACE processing by analyzing the singular values of the $\boldsymbol{R}$ matrix. Although QR factorization has an advantage in accuracy because it deals directly with the $\boldsymbol{H}$ matrix, it is not completely immune to ill-conditioning. If multiple columns of $\boldsymbol{H}$ are close enough to be linear combinations of each other, then this degradation will be reflected in $\boldsymbol{R}$ and its singular values.

The degree error variance and singular value decomposition are the two primary methods used in this thesis to evaluate the quality of a gravity field. In particular, these tools will be invoked to compare the gravity fields resulting from data collected during different spatial coverages. A more comprehensive description of this process and the other analysis that is undertaken in this thesis is described in the following section.

2.4 Data Processing Overview

The results obtained for this thesis follow a general data flow beginning with two sets of measurements from the satellites. The two measurement types are GPS double-differenced observations and K-band range rate data. This information is processed at the University of Texas at Austin's Center for Space Research using two programs to produce official gravity solutions that are released to the scientific community. The first program, the Multi-Satellite Orbit Determination Program (MSODP), takes the raw data and generates a REGRES file containing a set of observation residuals and partial derivatives. The REGRES file is passed to a second program, the Advanced

Equation Solver for Parallel Systems (AESoP) to obtain a linear least squares solution to the estimation problem, resulting in the harmonic coefficients that comprise the gravity solution. A more rigorous description of the procedure used to obtain gravity solutions from raw satellite data is located in Appendix C.

Much of the processing associated with this thesis involves taking a REGRES file associated with a particular month's worth of data and running AESoP multiple times to solve for gravity fields of different sizes for that month. In addition to a series of estimates for the harmonic coefficients, AESoP also produces the uncertainties associated with each estimate. These values are used to calculate the degree error variances across every degree for each solution according to Equation 2.16. The calibrated error estimates that are compared to these formal uncertainties are publicly available on JPL's Physical Oceanography Distributed Active Archive Center (PODAAC) website [15]. The degree error variance, which is ultimately the statistic that is being compared, is also calculated via Equation 2.16.

Another capability of AESoP is to produce the $\boldsymbol{R}$ matrix that is used in its QR factorization solution technique. As mentioned previously, $\boldsymbol{R}$ essentially contains the same information as $\boldsymbol{H}$ so its singular values are equally as useful. To calculate the singular values associated with $\boldsymbol{R}$, the LAPACK routine DGESVD is employed [3], which outputs a list of the values in descending order.

To accompany a study performed to visualize the spatial coverage during different conditions, a simulation is conducted to quantify this effect on the harmonic coefficient estimates. This was achieved using a modified version of a Fortran script provided by Srinivas Bettadpur. Based upon an input gravity field, the script creates a series of simulated observations to be made at various user-defined locations on the Earth's surface. It then attempts to re-solve for the harmonic coefficients using the previously determined values of the potential. This involves forming the $\boldsymbol{H}^T\boldsymbol{W}\boldsymbol{H}$ matrix, which involves the calculation of the measurement partial derivatives with respect to the normalized harmonic coefficients. Beyond this, the solution process utilizes the LAPACK routines DPPTRF, DPPTRS, and DPPTRI, which perform a Cholesky factorization of $\boldsymbol{H}^T\boldsymbol{W}\boldsymbol{H}$, solve a linear system of equations, and perform a matrix inverse, respectively [3]. The resulting set of harmonic coefficients reflects the ability of a hypothetical satellite to fully recover a field while only observing the potential at the user-defined locations.

The fundamental concepts behind the representation of Earth's gravity field, the associated perturbation frequencies, and ground tracks have been presented. In addition, the relevant tools that will be used to evaluate the various gravity solutions encountered throughout this thesis have been introduced and explained. Finally, a summary of the different processing techniques used to perform the analysis was provided. With the proper background information established, the properties of gravity fields under a variety of repeat conditions can now be assessed.

Chapter 3

Characteristics of Gravity Solution Degradation

This chapter examines the different ways in which the gravity field solutions for the GRACE mission are affected by repeat ground tracks. These consequences will be highlighted by comparing the results of the month containing the exact 61/4 repeat conditions (September 2004) with a preferable solution containing uniform coverage (February 2004). First, the degree error variance (DEV) plots associated with the different solutions will be compared. Next, the singular value decompositions (SVDs) of the $\boldsymbol{R}$ matrix are discussed.

Throughout the duration of the GRACE mission, there have been three major repeat ground track configurations corresponding to periods of 4, 5, and 7 days. As of the time of writing this thesis, GRACE is also passing through a 3-day repeat cycle. The relevent information associated with each repeat period (sorted by order of occurrence) is listed below:

Table 3.1: Significant Ground Track Repeat Dates for GRACE

Exact Repeat Date	Revolutions	Days
9/22/2002	76	5
9/19/2004	61	4
12/24/2009	107	7
5/17/2012	46	3

The 61/4 repeat in 2004 has been chosen to be the focal point of discussion, but the 5 and 7-day repeat cycles will be examined as well. The 61/4 period has been singled out because it has the shortest cycle of the group (excluding the 3-day, which hasn't ended yet), and therefore the degradation is anticipated to be the most severe. Theoretically speaking, the months surrounding September 19, 2004 provide the worst conditions for gravity recovery in the first decade of the GRACE mission. Therefore, the adverse effects associated with repeat ground tracks should be the most pronounced during this time.

3.1 Effects on Degree Error Variance (DEV)

As mentioned in Chapter 2, the degree error variance is a measure of the uncertainty associated with the estimated values of the harmonic coefficients for a given solution. That is, a set of coefficients with a relatively high DEV corresponds to a situation in which there is less confidence in the estimated gravity solution. The DEV plot is a useful representation of the statistics associated with an entire gravity solution, as well as the statistics of each individual harmonic degree. By comparing the DEV plots of different cases, conclusions can be drawn about how certain conditions have an effect on the resulting solution.

3.1.1 DEV During the 61/4 Repeat Period

The benefit of comparing the degree error variances of multiple gravity fields is demonstrated when the months surrounding the exact 61/4 repeat conditions are solved for and plotted. In addition, the gravity field from a time of uniform spatial coverage (in February 2004) can be included as a baseline to represent an "ideal" solution. The degree error variances of these months for a 120×120 field appear below in Figure 3.1.

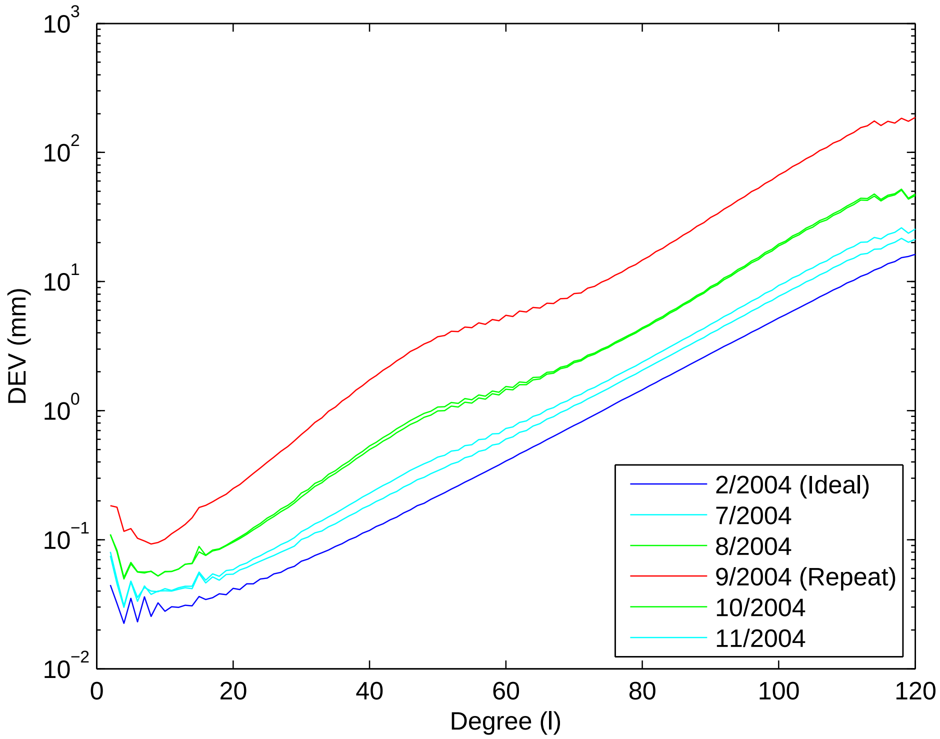

Figure 3.1: Degree error variances for a 120x120 field across different months in 2004.

A 120 × 120 field helps to emphasize the difference in the statistics of the ideal and repeat solutions. Figure 3.1 demonstrates that as the date of exact repeat is approached, the solution starts to degrade in the form of a higher DEV at all degrees. After GRACE reaches the exact repeat condition, the ground track slowly returns to a uniform density and the DEV of these subsequent fields is lower. A difference of a full order of magnitude of uncertainty is experienced between the ideal and repeat cases.

The Colombo-Nyquist rule dictates that the maximum size of a gravity field that can be determined during a repeat ground track without experiencing degradation is $L_{MAX} = \frac{R}{2}$. This suggests that shrinking the size of the estimated field will reduce the amount of degradation caused by the duplicate perturbation frequencies. Comparing the DEV plots of these gravity fields is a useful way to assess the validity of this claim. Using Figure 3.1 as a baseline, the effects of solving for a smaller gravity field can start to be seen with the solution of an 80 × 80 field, as in Figure 3.2.

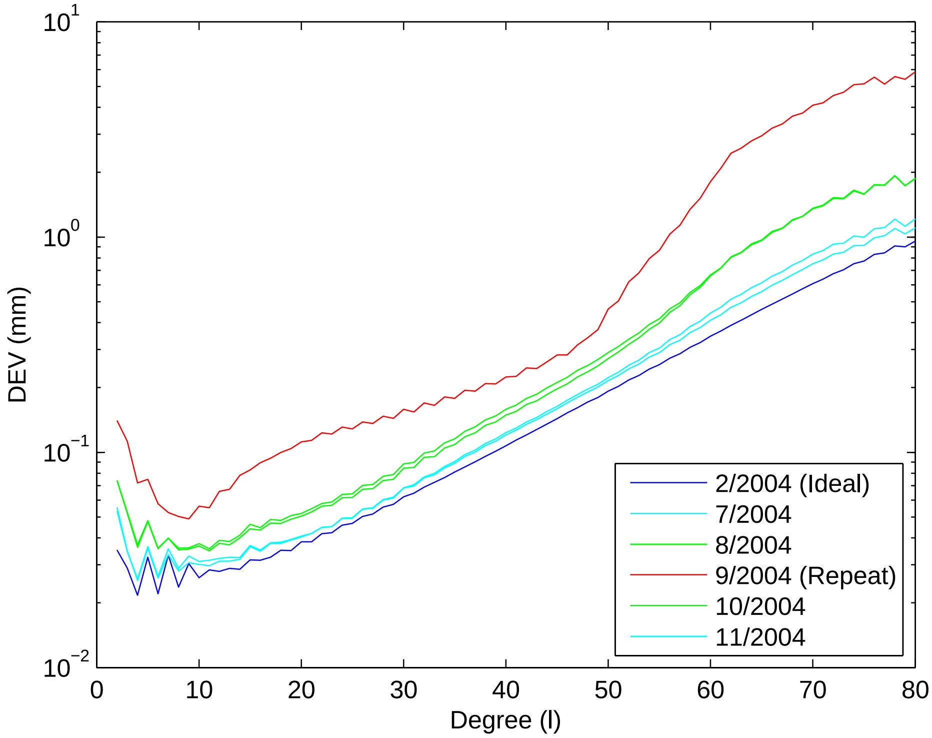

Figure 3.2: Degree error variances for an 80x80 field across different months in 2004.

One of the most drastic effects of a reduced solution size is that the DEV ranges are smaller for all months. Figure 3.2 also shows that there is less disparity in DEV between the different months. There is still a trend of increasing uncertainty as the exact repeat period is approached, but the effects of the degradation are less profound. When the field size is reduced even further to 30×30, there is virtually no difference in the DEV plots of the various months. This is illustrated in Figure 3.3.

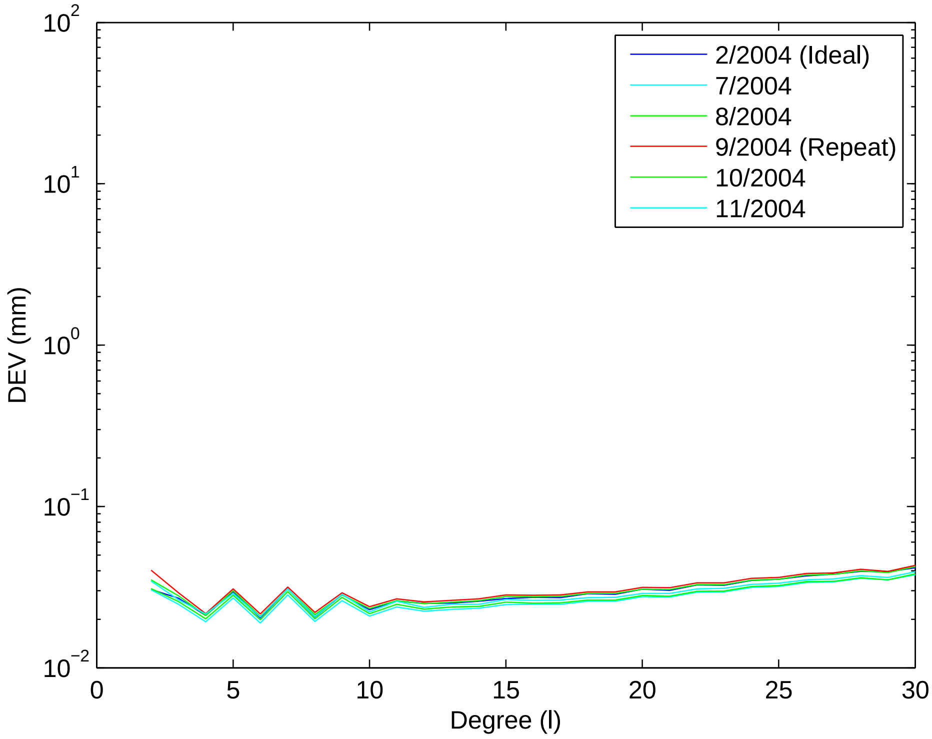

Figure 3.3: Degree error variances for a 30x30 field across different months in 2004.

In the case of larger field sizes such as in Figure 3.1, the solution during the repeat period experiences degradation relative to the ideal solution at all degrees. As the field size shrinks, the DEVs at the lower degrees (up to about degree 10) for the two cases start to more closely resemble each other. Once the field size is sufficiently low, the DEV of the repeat period solution tracks that of the ideal solution quite well for all degrees.

The observation that the harmful effects of repeat ground tracks can be essentially nullified by reducing the size of the gravity field solution is an important one. The idea that a gravity field size of $L_{MAX} = 30$ can be recovered with similar quality regardless of the spatial coverage (for a 61/4 repeat period) confirms the Colombo-Nyquist rule to a certain extent. However, although gravity fields larger than $L_{MAX} = 30$ show higher uncertainties, the fields with larger L_{MAX} produce solutions that are still of relatively good quality and released by the GRACE science team to the community [2]. With this in mind, identification of the largest field size to solve for during repeat periods before experiencing significant degradation becomes a topic of interest. To help determine this, the Figure 3.4 below displays the solutions of the various field sizes for the uniform and sparse ground track coverages.

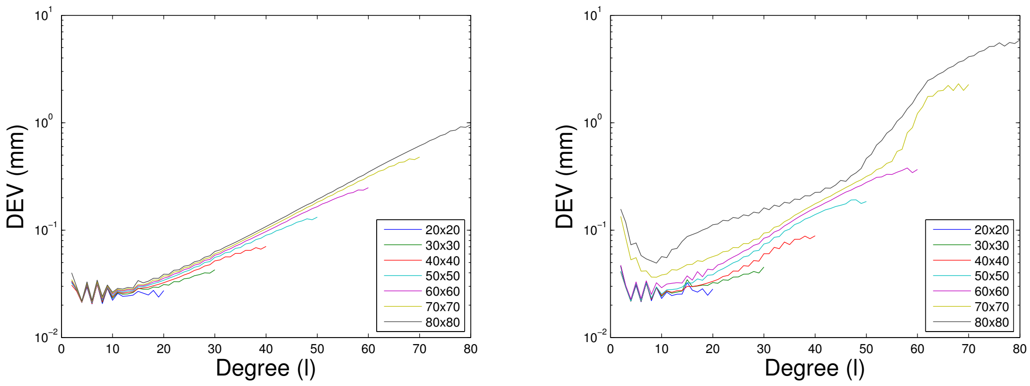

(a) February 2004

(b) September 2004

Figure 3.4: DEV for various field sizes during the (a) ideal and (b) repeat conditions in 2004.

There are a few different observations that can be made from Figures 3.4a and 3.4b. First, during a time when the ground track layout is relatively uniform, solving for larger field sizes has only a small detrimental impact on the quality of the solution in terms of DEV (as shown in Figure 3.4a) . As the field size grows, the DEV becomes slightly larger at degrees above 10, but this growth is much less profound than in the repeat case in September 2004, shown in Figure 3.4b. It can be seen from the degree error variance plots that the solutions are no longer well-behaved during repeat conditions. The solutions up to and including the 60 × 60 field follow the same general pattern as those in Figure 3.4a, but sudden degradation at all degrees is seen beyond this point. The ideal and repeat solutions up to $L_{MAX} = 60$ have been superimposed on top of each other for comparison in Figure 3.5.

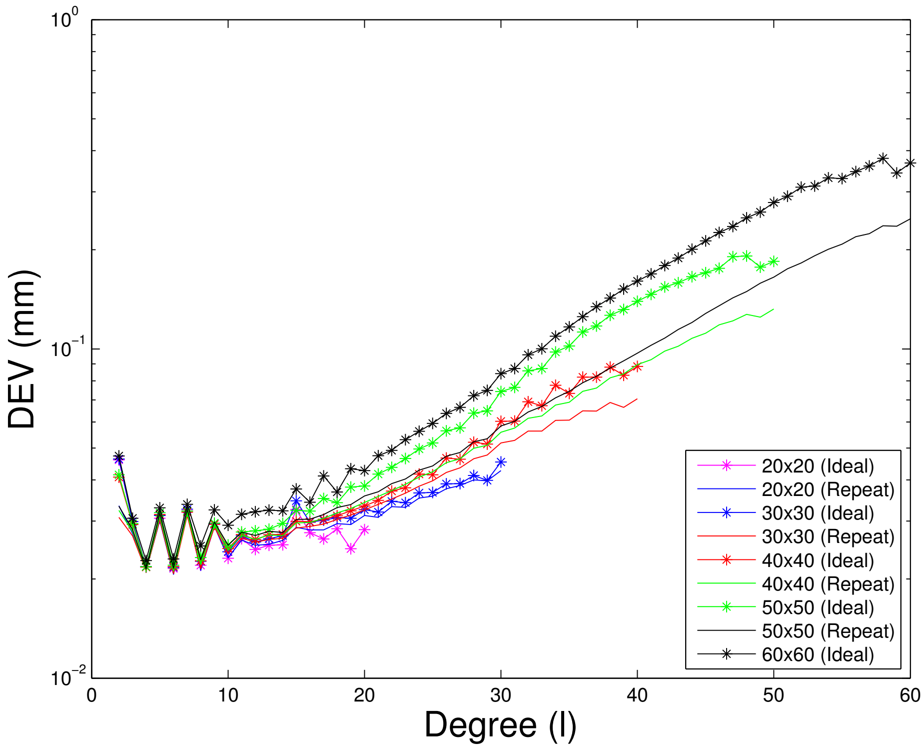

Figure 3.5: Degree error variances for $L_{MAX} = 20$, 30, 40, 50, and 60 during the ideal and repeat conditions in 2004.

Figure 3.5 shows that the disparity between uniform and repeat ground track solutions grows slightly when larger fields are estimated, but the same general shape is preserved up to $L_{MAX} = 60$. This is another reinforcement of Colombo's theory because the repeat period solutions above $L_{MAX} = 30$ are still worse than their ideal counterparts. However, these differences are tolerable until a specific field size is reached and major degradation occurs (between $L_{MAX} = 60$ and 70 for the case of the 61/4 repeat period). This result suggests that there is a link between the number of revolutions in the repeat cycle and the maximum field size that one can solve for during a repeat period without a significant drop in solution quality.

The analysis performed thus far has identified that there are in fact two "phases" of solution degradation that occur during a repeat ground track. The first phase is known as "minor degradation" and coincides with the field size that the Colombo-Nyquist rule predicts will pose problems for the gravity recovery problem, which is $L_{MAX} = \frac{R}{2}$. However, it has been shown in Figure 3.5 that the increased uncertainty around these field sizes is not catastrophic. This conclusion will be reinforced quantitatively in the next chapter, where the uncertainty levels are compared to those of the calibrated error estimates. The most severe drops in solution quality can be seen to occur around the field sizes where $L_{MAX} = R$, as seen in Figure 3.4b. This is the scale of degradation that the Colombo-Nyquist rule expects for $L_{MAX} = \frac{R}{2}$ and will be referred to as the phase of "major degradation". These observations play a key role in the data analysis of this thesis and will be touched upon several times in the future sections.

3.1.2 Corroboration for Other Repeat Periods

To emphasize the relationship between the onset of degradation and severity of the repeat ground track, the degree error variance plots of the other major repeat periods experienced by GRACE are considered, particularly the 7-day cycle during December of 2009. As with the 4-day repeat period, a month of uniform coverage (August 2010) was included for comparison. The degree error variances of these two months, as well as the months surrounding the repeat period, were obtained for solutions having $L_{MAX} = 120$. The corresponding DEV plots are shown in Figure 3.6.

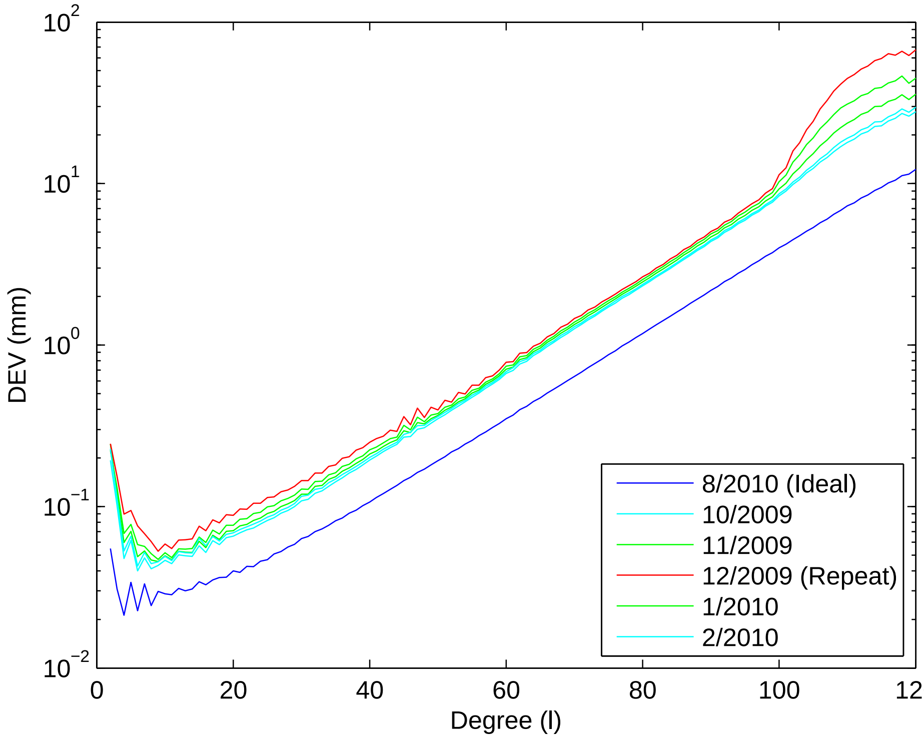

Figure 3.6: Degree error variances for a 120x120 field across different months in 2009.

This repeat cycle is longer than the one in September 2004, meaning it has more revolutions associated with it (107). Therefore, the 120×120 field size is still large enough to experience degradation, but there is less of a disparity between the DEV of the ideal and repeat months than in the 4-day solutions. The degrees up to $l \approx 100$ are well-behaved even during the month containing the exact repeat, and then the DEV jumps by an order of magnitude at the highest degrees. The underlying observation from Figure 3.6 is that a relatively large field ($L_{MAX} = 120$) has less of a negative impact during longer repeat periods. A better idea of the smallest field size that experiences a decrease in quality is achieved by comparing the DEV plots of multiple field sizes for the two different ground track densities. This is illustrated in Figure 3.7.

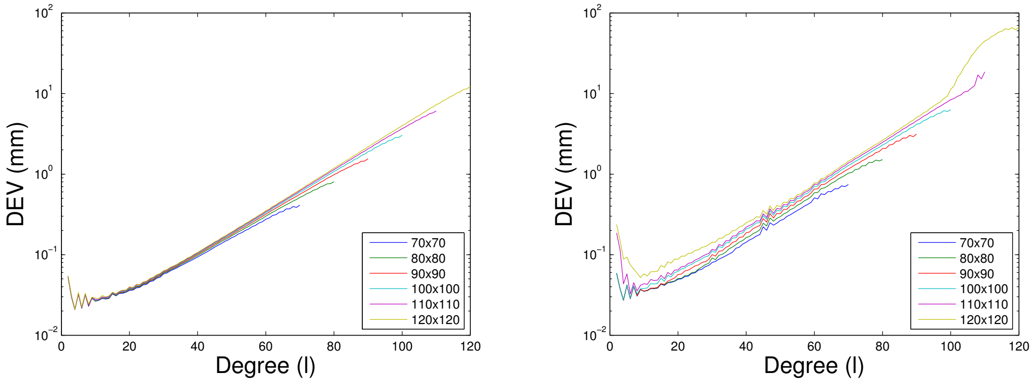

(a) August 2010

(b) December 2009

Figure 3.7: DEV for various field sizes during the (a) ideal and (b) repeat conditions in 2009/2010.

This study is similar to that which was done for the 61/4 repeat conditions in Figure 3.4. However, the solutions for February 2004 experienced problems soon after $L_{MAX} = 60$. For the 107/7 repeat condition, the DEV resembles its ideal counterpart fairly closely until $L_{MAX} = 110$, which reinforces the observation that the maximum field size that can be solved for during a repeat ground track is roughly the number of revolutions in the cycle. The larger solutions of the ideal and repeat months are included in Figure 3.8 for comparison.

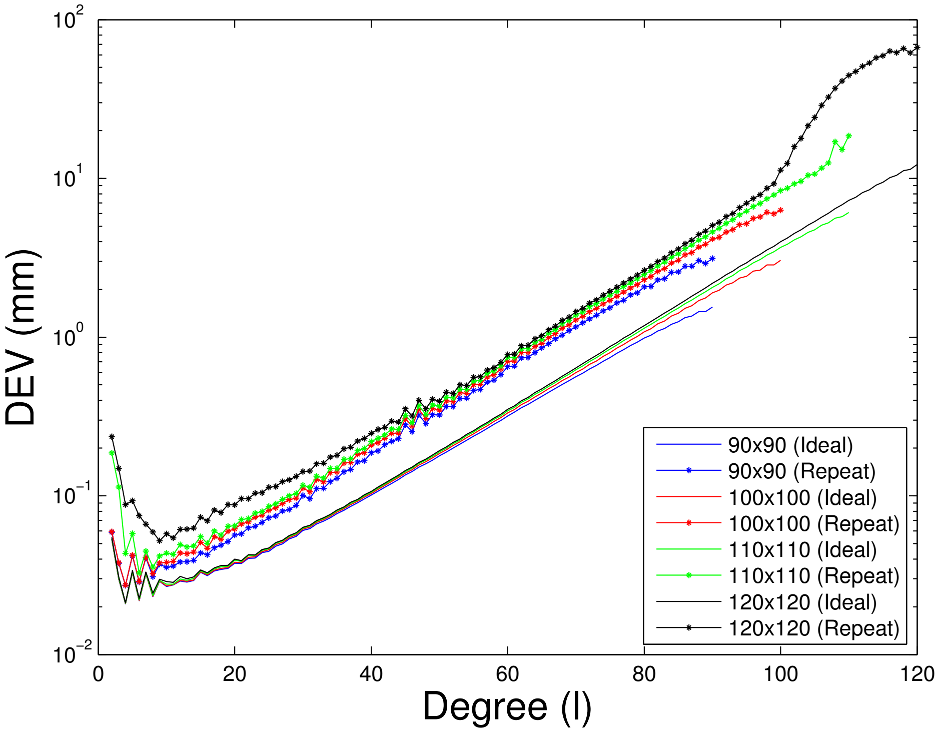

Figure 3.8: Degree error variances for $L_{MAX} = 90$, 100, 110, and 120 during the ideal and repeat conditions in 2009/2010.

Figure 3.6 hinted that the extent to which large fields were subject to poor results was dependent on the "severity", or lack of spatial resolution, of the ground track conditions. The shorter repeat periods (such as the 4-day repeat in 2004) were affected significantly, while the 7-day solutions were still relatively well-behaved. This relationship is confirmed by plotting the degree error variances of a 120 × 120 field for the different months containing the exact repeat periods together, shown in Figure 3.9.

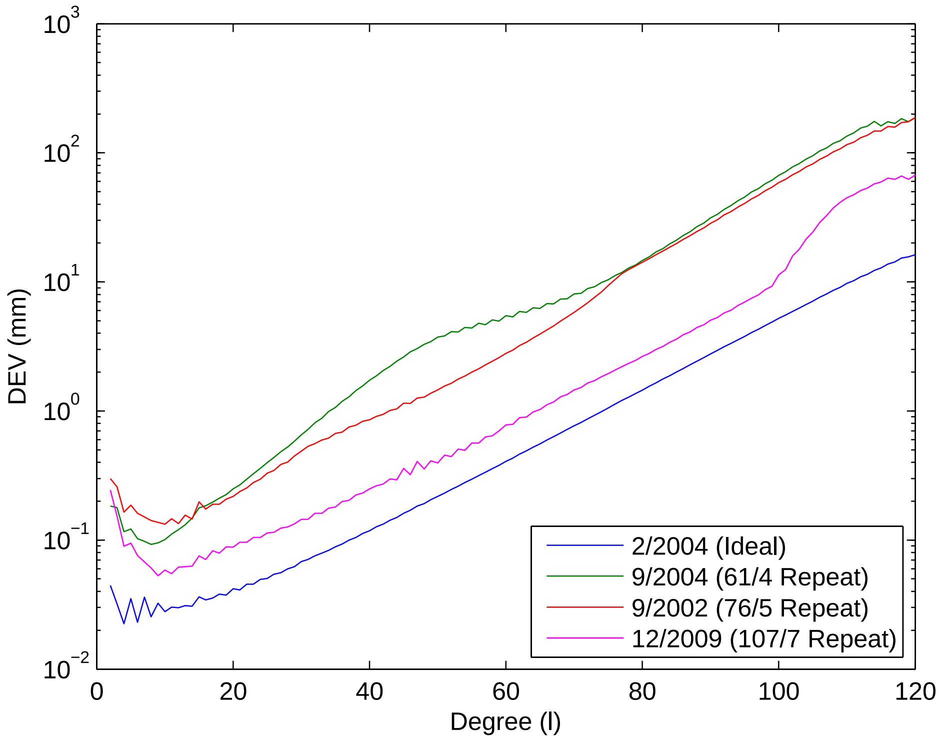

Figure 3.9: Degree error variances for a 120x120 field for uniform and various repeat periods throughout the GRACE mission's lifetime.

As expected, the 4 and 5-day cycles show roughly an order of magnitude more uncertainty than usual in the estimates of the harmonic coefficients at all degrees in the solutions. However, the 7-day repeat period, containing 107 revolutions, is only slightly degraded relative to the ideal case for a majority of the of the solution (roughly the first 100 degrees).

To reiterate upon the analysis performed thus far, there has been an identification of two field sizes beyond which varying levels of solution degradation are encountered. By examining these effects over various repeat periods, the points of degradation are confirmed to be dependent on the number of revolutions of the satellite in the repeat cycle, namely at $L_{MAX} = \frac{R}{2}$ and $L_{MAX} = R$. This observation is reinforced in the following section, which addresses the singular values associated with the estimation problem.

3.2 Behavior of Singular Values and Condition Numbers During Repeat Ground Tracks

Recall that the number of nonzero singular values of a particular matrix of interest is equivalent to its rank. Because $\boldsymbol{R}$ contains the information from $\boldsymbol{H}$ and $\boldsymbol{W}$, its singular values provide information about the numerical conditioning of the estimation problem. When there is a reduction in observability, the $\boldsymbol{R}$ matrix still experiences some of the same numerical problems as $\boldsymbol{H}$. Performing a singular value decomposition (SVD) on $\boldsymbol{R}$ helps to diagnose the root of the issue and is often the first step in circumventing these numerical pitfalls.

3.2.1 Singular Values During the $61/4$ Repeat Period

As mentioned in Chapter 2, the estimation of gravity fields using GRACE data is considered to be a discrete ill-posed problem, meaning that there is a smooth transition between the highest and lowest singular values. This characteristic is displayed in Figure 3.18 when the singular values of 120 × 120 solutions pertaining to February and the months surrounding the repeat period are plotted.

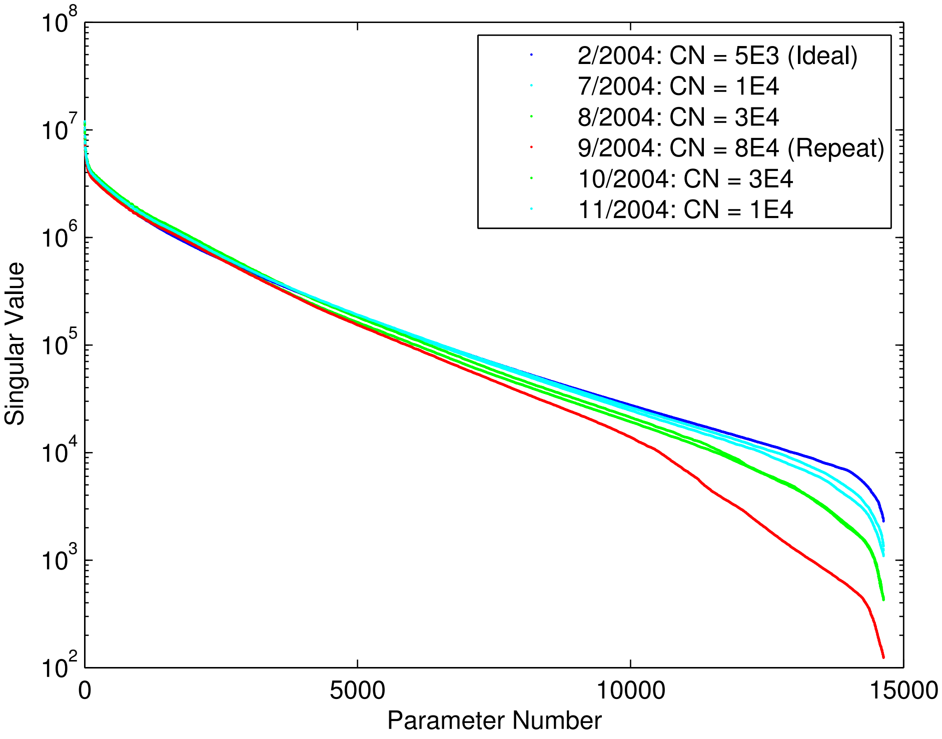

Figure 3.10: Singular values associated with the paramater sets in a 120 × 120 field for different months in 2004.

The degradation associated with the GRACE orbit's transition to a repeat ground track is also apparent in the singular value curves. The ideal layout produces a "shape" of singular values that gradually shifts from higher to lower values. As the exact repeat conditions are approached, the shape of the curve becomes more jagged and smaller singular values appear at the low end of the spectrum. Regardless, the lowest values in all of the cases are not especially close to zero, meaning the estimation problems are not numerically rank deficient. Despite this, the solutions near the exact repeat period are more sensitive to changes, as indicated by the higher condition number. Since the highest singular values are unaffected by the ground track layout, the resulting condition number is about an order of magnitude higher during the 61/4 repeat ground track than it is during an ideal month.

As with the DEV plots in Figure 3.4, the singular values for the uniform layout in February 2004 were calculated for multiple field sizes and considered to be the ideal case. The same field sizes were obtained for the month of September so that a comparison could be made. This enables the effect of field size on the singular values during a repeat period to be observed, as shown in Figure 3.11.

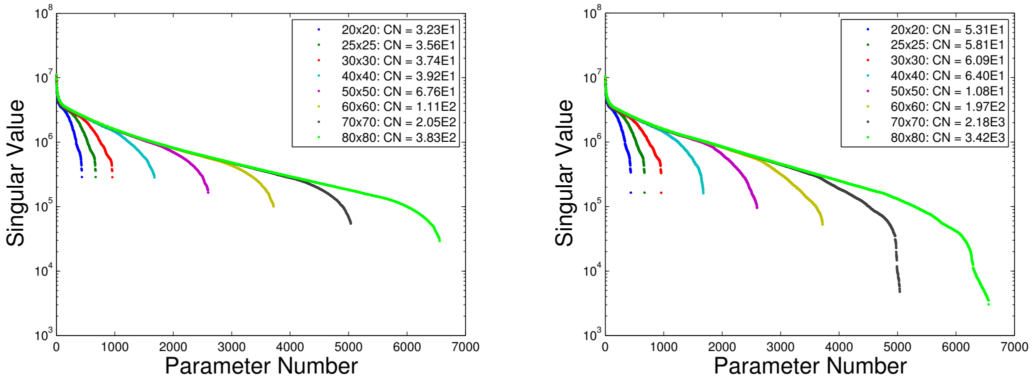

(a) February 2004

(b) September 2004

Figure 3.11: Singular values of $\boldsymbol{R}$ between $L_{MAX} = 20$ and 80 during the (a) ideal and (b) repeat conditions in 2004.

There are two major trends that can be identified from the comparison of Figures 3.11a and 3.11b. First, the singular values for $L_{MAX} = 20$, 25, and 30 appear to be independent of the field size, regardless of the spatial coverage. Also, the sets of singular values for these solutions are very similar for the ideal and repeat cases, with the exception of the lowest singular value. For the 40×40 field and beyond, smaller singular values start to appear as the field size grows. This transition will be addressed shortly. The larger singular values remain relatively unchanged, so the condition number steadily grows with larger field sizes, but not at a very significant rate. The singular value plots in February exhibit the same general shape regardless of L_{MAX}, which is not the case during the repeat period in Figure 3.11b. The field sizes in which degradation occurs can be seen quite clearly when examining these singular values. Coincident with the DEV results, the first sign of major degradation (in the form of extremely low singular values) appears beyond $L_{MAX} = 60$. The shape of the solutions beyond this are a departure from the smooth curve associated with the well-behaved cases in February. Due to the appearance of lower singular values, the condition numbers of the larger field sizes jump to roughly an order of magnitude higher than their "ideal" counterparts in Figure 3.11a. The higher condition numbers confirm that the harmonic coefficient estimates during September 2004 are more susceptible to numerical errors, especially at fields greater than $L_{MAX} = 60$. Figure 3.12 provides a look at the solutions of field sizes near the expected threshold of degradation (the number of revolutions in the repeat period) in order to help explain the behavior.

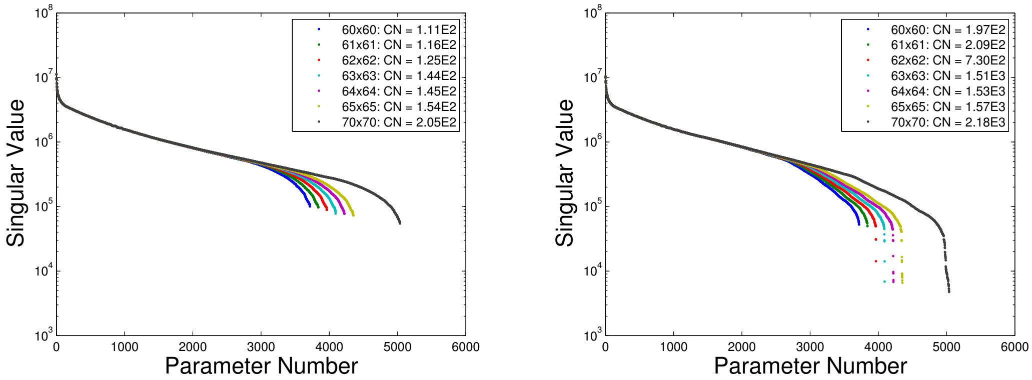

(a) February 2004

(b) September 2004

Figure 3.12: Singular values of $\boldsymbol{R}$ between $L_{MAX} = 61$ and 65 during the (a) ideal and (b) repeat conditions in 2004.

The ideal ground track layout in Figure 3.12a closely follows the trend that it exhibited in Figure 3.11a, which was expected. However, the results in

September show an interesting pattern starting with the 62×62 field, where the singular value “anomalies” start to arise. First, this reinforces the observation that the significant solution degradation begins in the field sizes just beyond the number of revolutions in the repeat cycle. Also, the number of these anomalies grows with an increase in L_{MAX}.

The transition in gravity field size to $L_{MAX} > R$ has shown to be a critical point in the numerical conditioning and associated solution quality. There is also an earlier point in the singular value plots (roughly around $L_{MAX} = \frac{R}{2}$) that warrants attention. The solution sizes in this region are displayed for February 2004 and September 2004 in Figures 3.13a and 3.13b, respectively.

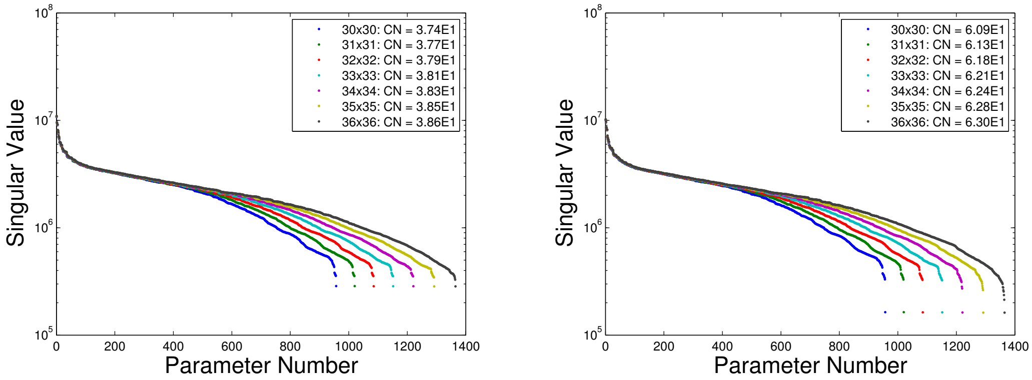

(a) February 2004

(b) September 2004

Figure 3.13: Singular values of $\boldsymbol{R}$ between $L_{MAX} = 30$ and 36 during the (a) ideal and (b) repeat conditions in 2004.

Recall in Figure 3.11 that the singular values of the solutions up to about $L_{MAX} = 40$ were relatively the same for the respective months. As the solution size reaches $L_{MAX} = 34$, smaller singular values start to appear for the month of September, but not for the ideal case in February. However, the existence of one relatively small value in both months causes their condition numbers to remain essentially the same. As the field size grows to about 40×40, the newest singular values in September approach the lowest existing singular value and eventually even lower values appear, rendering it insignificant. The result is the gradual downward trend and rise in condition number beyond $L_{MAX} = 40$ in Figure 3.11. Although the condition number is unaffected at first by the emergence of lower singular values in Figure 3.13b, this is evidence that the estimation problem is starting to become less well-conditioned around $L_{MAX} = \frac{R}{2}$. Oddly enough, the ideal case in Figure 3.13a exhibits this behavior around the same point, but to a lesser extent.

3.2.2 Comparison of Singular Values for Different Repeat Periods

As with the degree error variances, other repeat periods were considered in order to verify the relationship between the number of revolutions in the repeat period and the onset of significant degradation. Essentially the same gravity field solution sizes as in Figure 3.11 were computed for the 107/7 repeat period in December 2009 and an "ideal" period in October 2010. The singular values associated with these solutions are shown below in Figure 3.14.

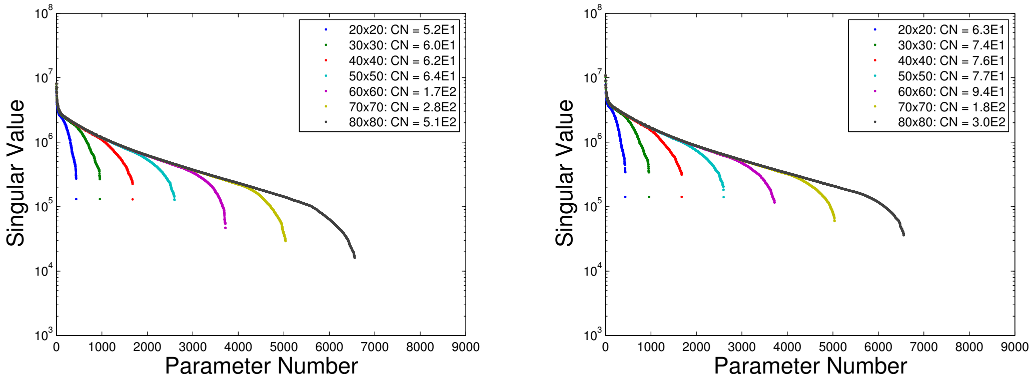

(a) October 2010

(b) December 2009

Figure 3.14: Singular values of $\boldsymbol{R}$ during the (a) ideal and (b) 7-day repeat conditions in 2009/2010.

Very small singular values started to appear for the fields that were $L_{MAX} = 70$ and higher in Figure 3.11b, but this is not the case with the month containing the exact 107/7 repeat in Figure 3.14b. The ideal and repeat singular values look very similar, and although the singular values during the repeat period are slightly lower than those in the ideal case at higher degrees, there are no distinct outliers that are indicative of significant degradation. The observation that anomalistic singular values and therefore ill-conditioned problems occur at different field sizes for different repeat periods provides further evidence that degradation is related to the length of the corresponding repeat period (and therefore the number of revolutions). Since this particular example is centered around the 107/7 period, the singular values of field sizes up to 120×120 are now considered. The singular values associated with field sizes of $L_{MAX} = 80$, 90, 100, 110, and 120 are displayed in Figure 3.15.

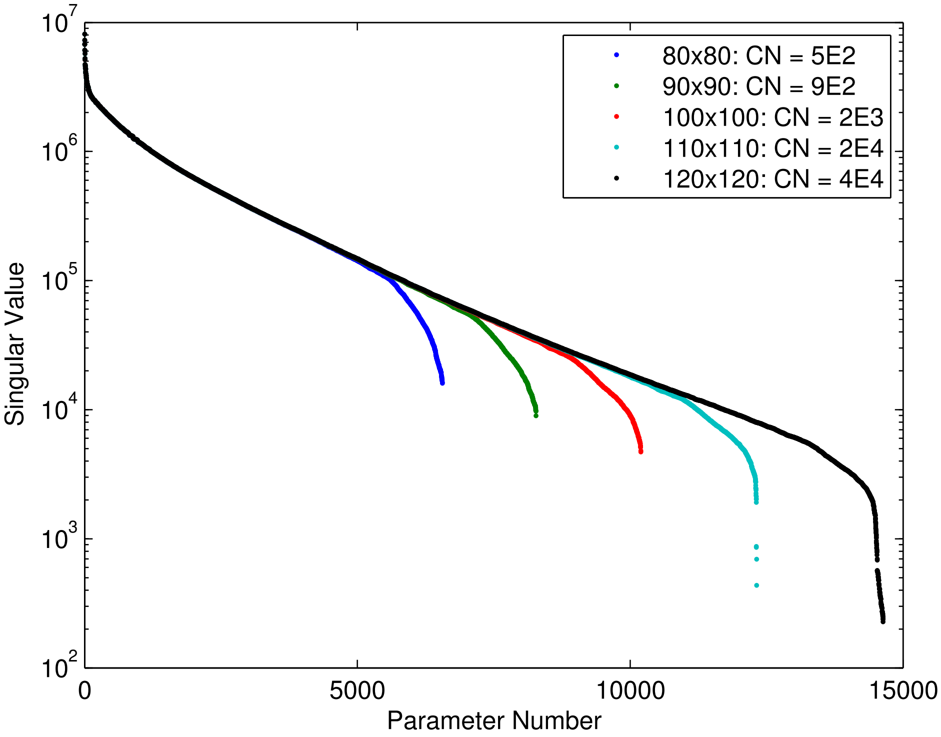

Figure 3.15: Singular values of $\boldsymbol{R}$ during the 107/7 repeat condition in 2009.

As expected, the now-familiar stray singular values have appeared starting with a solution having $L_{MAX} = 110$. Figure 3.16 shows the intermediate fields between 100×100 and 110×110. Upon inspection, the first evidence of ill-conditioning occurs at $L_{MAX} = 107$.

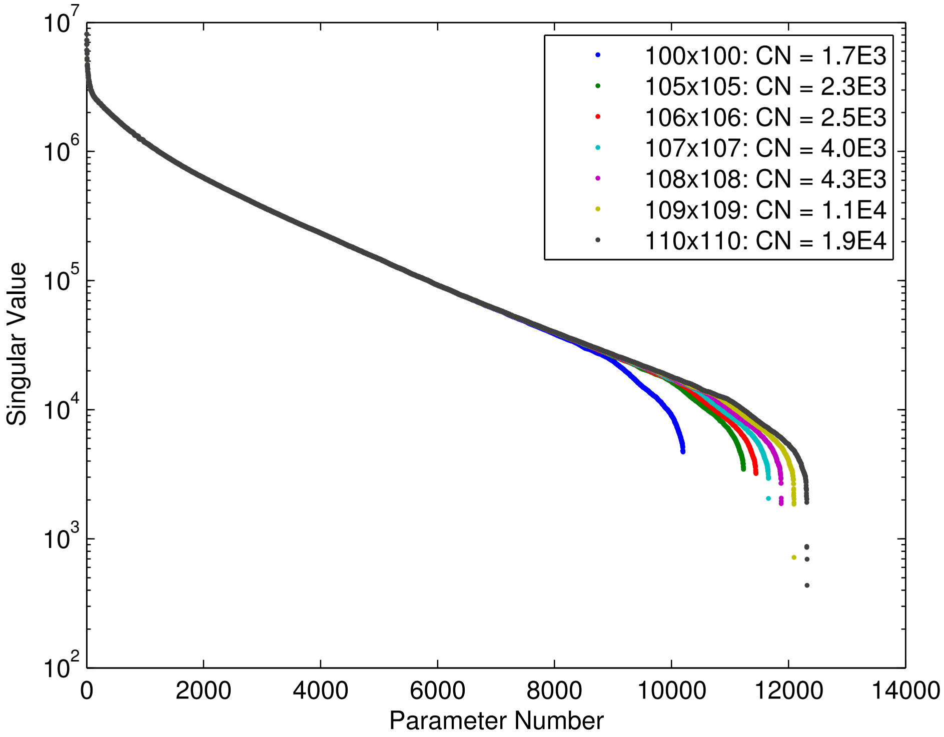

Figure 3.16: Singular values of $\boldsymbol{R}$ during the 107/7 repeat condition in 2009.

These results coincide quite well with the number of revolutions completed by GRACE in the repeat cycle during 2009. The relationship between the threshold of significant degradation and the sparsity of the ground track layout is even further supported by observing this behavior for the second time. The trend involving the onset of lower singular values around $L_{MAX} = \frac{R}{2}$ is also seen during this repeat period, as shown in Figure 3.17.

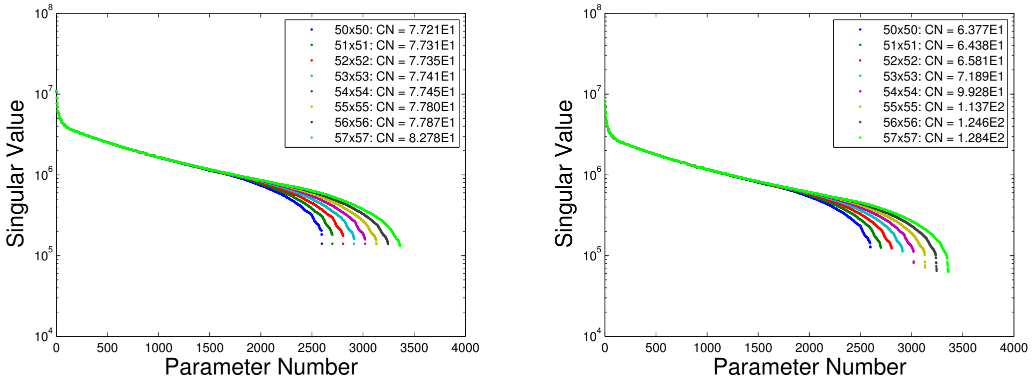

(a) August 2010

(b) September 2009

Figure 3.17: Singular values of $\boldsymbol{R}$ during the (a) ideal and (b) repeat conditions in 2009/2010.

As with the 61/4 repeat period in Figure 3.11, both the uniform and sparse ground track layouts contain one low singular value up to a certain field size ($L_{MAX} \approx 50$ in this case). Beyond this point, lower singular values start appearing with an increase in L_{MAX} and eventually "surpass" the lone singular value. This occurs around $L_{MAX} = 53$ for September, which is essentially half of the number of revolutions in the repeat cycle. Fields larger than this begin to produce even lower singular values, causing the condition number to grow.

The singular values of the 107/7 repeat period were relatively well-behaved (only experiencing minor degradation) up to around $L_{MAX} = 100$, while the solutions during the 61/4 conditions were severely affected. This suggests that for a given field size that is relatively large, a longer repeat cycle will yield better results than a short period with a very sparse ground track. This relationship is illustrated in 3.18 by plotting the singular values of a 120×120 gravity solution for the various repeat periods that GRACE has passed through.

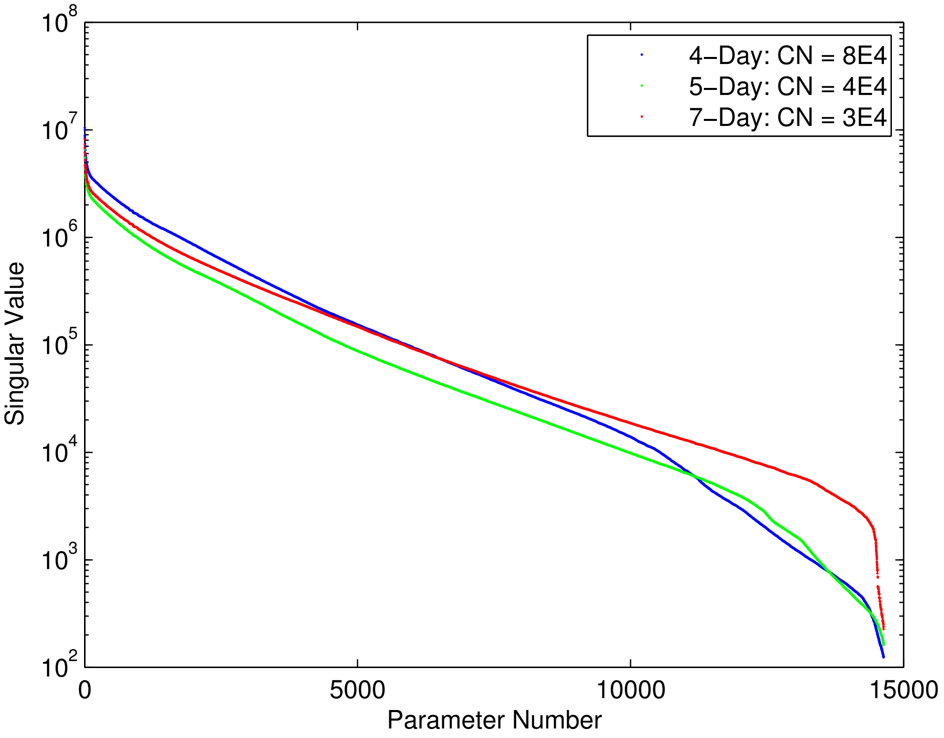

Figure 3.18: Singular values of $\boldsymbol{R}$ during several repeat periods for a 120×120 field.

The singular value plots for all repeat periods in Figure 3.18 have experienced degradation, as expected. However, the extent to which the solutions have been affected varies with the length of the repeat cycle. The 61/4 period in 2004, which is the shortest, appears to suffer the most when recovering a large gravity field. The 7-day cycle has relatively few small outliers and they are not quite as low as the other data spans. This relationship is also reflected in their condition numbers, with the highest (and most ill-conditioned) one associated with the 4-day repeat period.

When the field size is reduced to $L_{MAX} = 30$, which should theoretically be totally observable during all of these periods, the singular value plots have similar shapes and condition numbers. These plots are shown below in Figure 3.19.

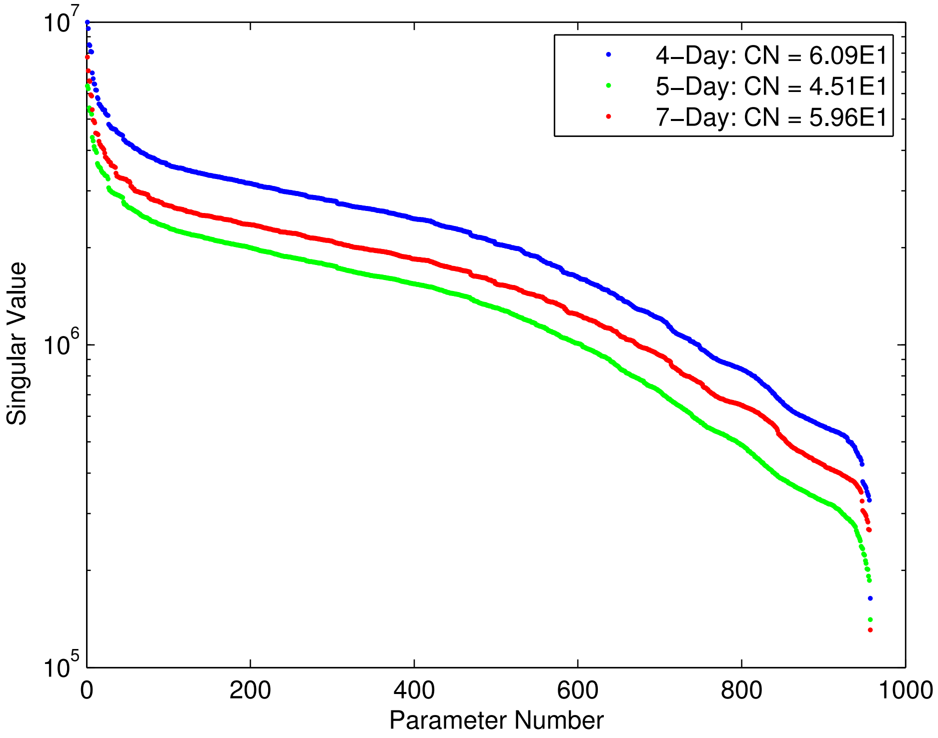

Figure 3.19: Singular values of $\boldsymbol{R}$ during several repeat periods for a 30 × 30 field.

When the estimation problem to determine the gravitational coefficients is well-conditioned, the ground track geometry has virtually no effect on the quality of the solutions. In fact, the solution for the 7-day period has worse results than the 5-day period for this particular field. This is evidence that spatial coverage is no longer a major source of solution degradation at this point and that other external factors become the primary contributors.

3.2.3 The Variation of Condition Number with Solution Size

Throughout the analysis of the singular value plots, the condition number has been a simple indicator of the quality of a gravity solution. The higher condition numbers corresponded to problems that were less well-behaved numerically, leading to a gravity field with higher overall uncertainty. By observing the evolution of the condition number as the estimated field size grows, the points at which the quality of the solution become significantly affected become apparent. The relationship between the size of the solution and the condition number for different ground track densities is illustrated in Figure 3.21.

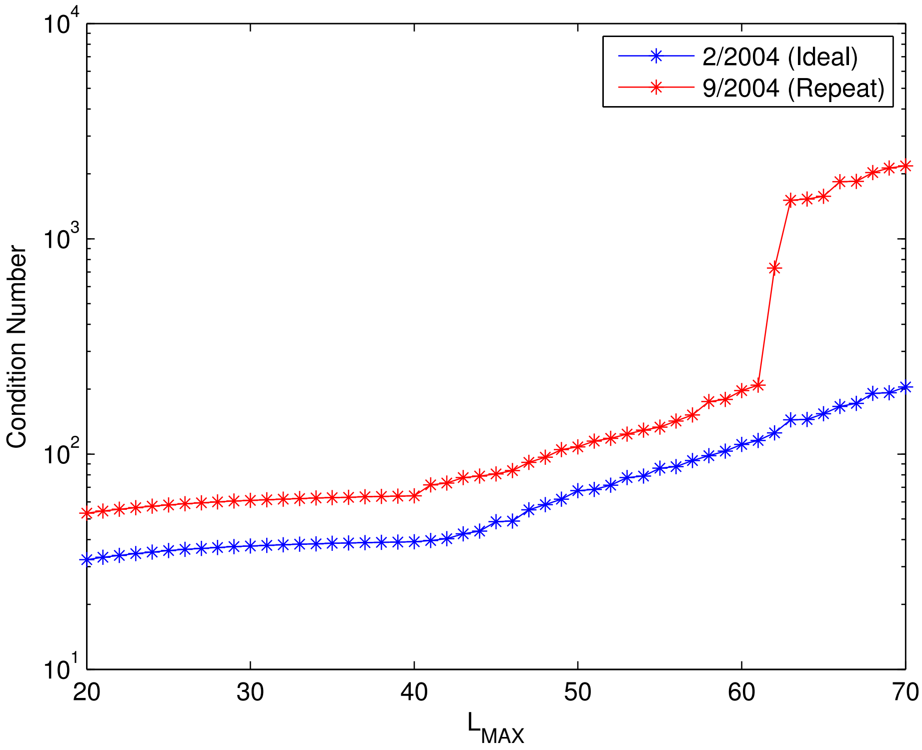

Figure 3.20: Condition numbers associated with gravity solution sizes for February and September 2004.

For the uniform coverage in February 2004, the condition number steadily increases beyond degree 40, but not very much. The condition numbers for the repeat case closely match those in the ideal case up to degree 40, but then start to slightly diverge away, even though those in the ideal case are rising as well. Once $L_{MAX} = 62$ is reached, the repeat case condition number jumps sharply, while the ideal case is essentially unaffected. This is consistent with the field sizes for which the other plots were starting to see substantial amounts of degradation, which is the number of revolutions in the repeat period. The point at which the two solutions start to diverge ($L_{MAX} = 41$) can be related to the minor degradation that was illustrated earlier. The appearance of lower singular values did not affect the condition number of the solution until this point because of the existence of the low anomaly. Once the newest singular values were lower than this value (at $L_{MAX} = 41$), the condition number rose steadily until severe degradation occurred.

These two "phases" of solution degradation and their relationship to the number of revolutions in the repeat cycle can be visualized in Figure 3.21 below.

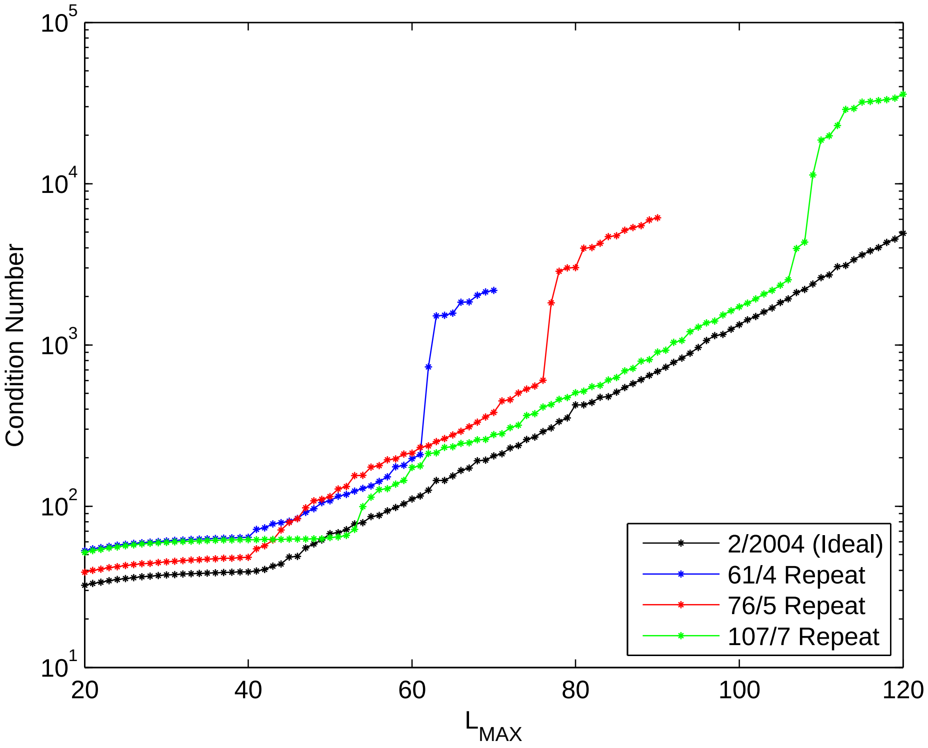

Figure 3.21: Condition numbers associated with gravity solution sizes for ideal and repeat conditions.

The ideal case of uniform coverage sees a gradual rise in condition number with increasing field size. This is most likely due to the attenuation of the signal at higher degrees, naturally leading to more uncertainty in the estimated solution. For the repeat periods, the onset of minor and major degradation occur at field sizes that are dependent on the number of revolutions in the repeat cycle. The minor phase begins around $L_{MAX} = \frac{R}{2}$ and the major phase starts at $L_{MAX} = R$.

Thus far, the general behavior of gravity solutions during repeat ground tracks has been identified by observing the difference between "ideal" and degraded scenarios. The quality of the solutions during repeat ground tracks has been shown to be consistently worse according to the analysis tools described in Chapter 2. The degree error variances associated with the repeat periods are considerably higher than during periods of adequate coverage for large gravity fields, indicating a poorer solution. However, when the field size is reduced to $L_{MAX} = \frac{R}{2}$, the solution is virtually unaffected by the spatial coverage achieved during that month and the degree error variances are very similar. Beyond this field size and up until $L_{MAX} = R$, the solutions are not degraded substantially enough to be considered unusable. However, beyond $L_{MAX} = R$ the uncertainties corresponding to the estimated harmonic coefficients are distinctly higher than usual. These two points are considered to be the thresholds of minor and major degradation for the months containing a repeat ground track.

This pattern is also observed in the singular values of the $\boldsymbol{R}$ matrix used in the estimation process. Lower singular values, which lead to worse numerical conditioning, start to appear at the onset of minor degradation. When major degradation occurs, extremely low singular values exist and the condition number sharply rises, indicating that the underlying estimation problem used to determine the gravity field is starting to break down.

Data from other months (containing the 76/5 and 107/7 and repeat ground tracks) was used to help validate the aforementioned results. Similar behavior in the DEV and singular value plots was identified, but the degradation was observed at different field sizes than the original 61/4 ground track. The thresholds of degradation were consistent with the previous data span in that they occurred at $L_{MAX} = \frac{R}{2}$ and $L_{MAX} = R$, reinforcing the notion that the "severity" of the ground track has an impact on the maximum size of a high quality solution.

The detrimental effect of reduced coverage on the ability to recover certain gravity fields has now been characterized in multiple ways. In the next chapter, the underlying reasons for why this occurs will be addressed.

Chapter 4

Sources of Degradation

Chapter 3 documented the ways in which different aspects of the gravity solution process were affected when GRACE passes through a repeat ground track. Compared to the ideal uniform layout, the reduced spatial coverage was shown by all of the methods used to evaluate a gravity field to lead to some form of degradation. As a result, the general effects of repeat orbits are now fairly well established, but the nature of these effects still needs to be determined. The following sections will attempt to explain some of the physical and computational reasons for why this degradation occurs.

4.1 Spatial Coverage During Repeat Periods

As previously mentioned, the repeat ground configuration is undesirable for geodetic satellites because they only pass over a small portion of the Earth's surface. This translates to only observing a particular aspect of the Earth's gravity field, making the determination of high fidelity solutions difficult. To demonstrate this, the surface of the Earth was divided into sections (or "bins") that are 3° latitude by 3° longitude. For the months of February and September 2004, the number of times GRACE crossed through each of these bins was counted. In Figure 4.1, these passes were plotted as a function of geographic location to visualize the spatial information of the gravity field that was available.

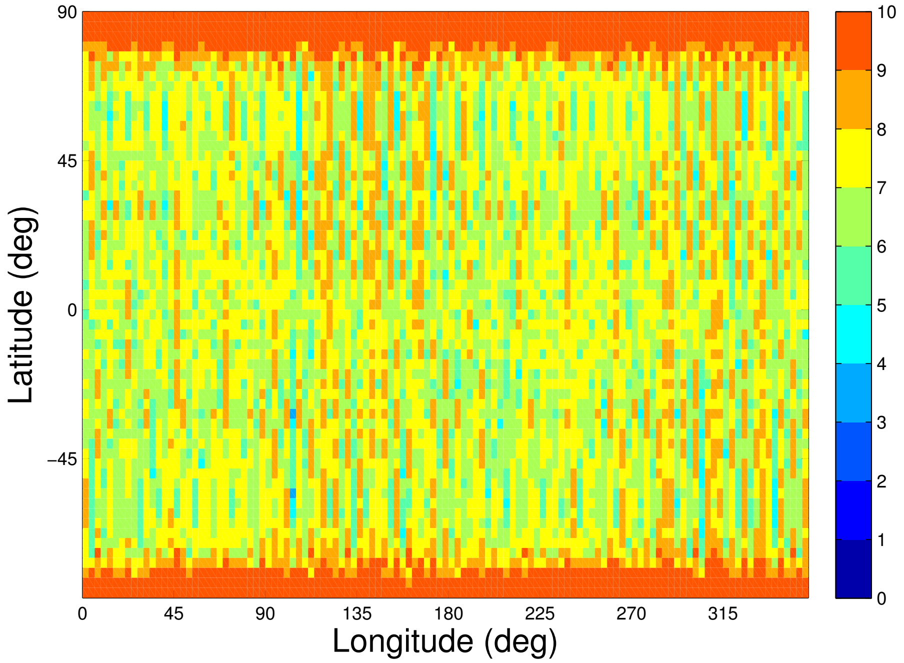

Figure 4.1: Number of passes through 3° × 3° bins during February 2004.

Figure 4.1 represents the ideal scenario that has a uniform ground track layout. During this month, GRACE is passing over every section of the Earth at least five times (with a few exceptions), which is sufficient information to produce an accurate depiction of its gravity field to a relatively high resolution. There were many passes through the polar regions, with some sections containing over 60 crossings. However, as Figure 4.2 shows, this global observability is lost during the 61/4 repeat conditions.

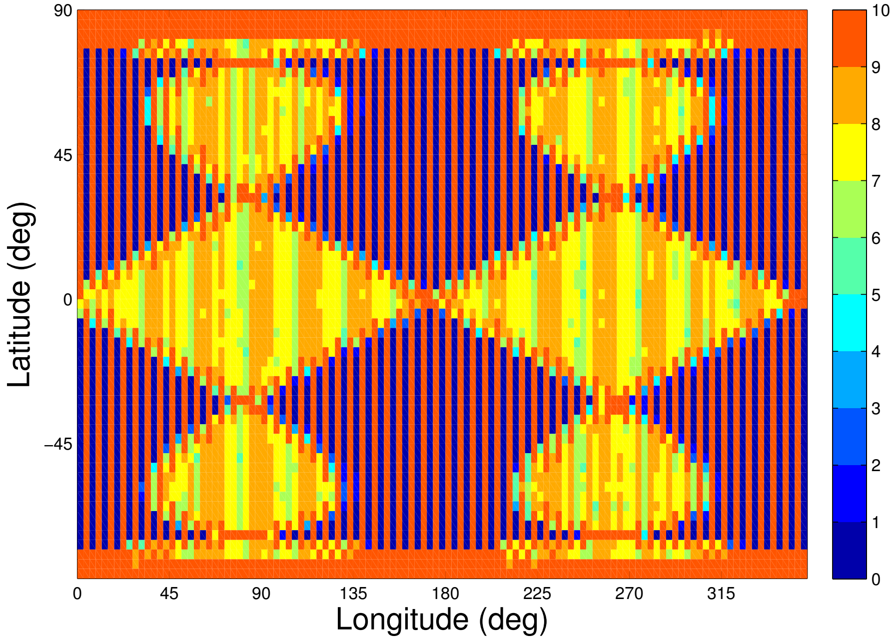

Figure 4.2: Number of passes through 3° × 3° bins during September 2004.

The high inclination of the GRACE mission's orbit still leads to adequate coverage at the poles, but there are many regions of the Earth that contain no observations. However, there are bands of longitude that experience many passes (in fact, more than the uniform layout). Not surprisingly, this is directly related to the orbital geometry orbit during repeat conditions. The size of the "bins" in this example play an important role in that there is a link between the degree to which the field can theoretically be resolved and the resolution of the grid, which defines the bins that all must contain observations. The bin size is ultimately dependent on the spacing (in degrees) between ascending node crossings, so the relationship between these two quantities can be described by:

$$L_{MAX} = \frac{180^\circ}{\Delta\lambda} \tag{4.1}$$

where $\Delta\lambda$ corresponds to an increment in longitude (and alternatively the bin size). Therefore, a grid consisting of $3^\circ \times 3^\circ$ bins will indicate that a field of $L_{MAX} = 60$ can be successfully determined if there are passes through all of the bins. This observation is confirmed by the plots of the uniform and repeat coverages shown in Figures 4.1 and 4.2, respectively. The uniform case has passes through every bin and fields larger than 60×60 can be resolved. However, the repeat field has bands at certain longitudes that are never passed over during the month, and the resulting solution at $L_{MAX} = 60$ is adversely affected. By decreasing the size of the bins to $2^\circ \times 2^\circ$, a monthly solution having passes in each of the bins will be able to resolve a 90×90 field. The coverage during ideal month of February is now shown in Figure 4.3 below.

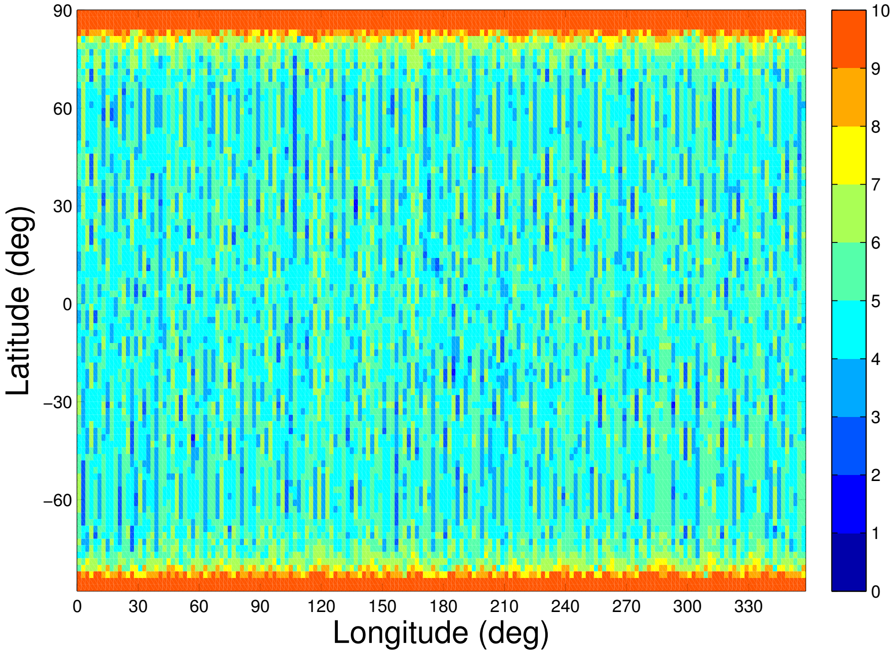

Figure 4.3: Number of passes through 2° × 2° bins during February 2004.

Even when the bins are smaller, the uniform coverage obtained during this ideal layout is sufficient to have a pass through every bin (although the number of passes through each bin has been generally reduced). The ability to adequately recover a gravity field to degree and order 90 during this period has been well-established from Chapter 3, and it is reflected in this bin study. The 61/4 repeat configuration, which had "unobserved" 3° × 3° bins, shows even worse coverage when the bins are smaller. This behavior is displayed below in Figure 4.4.

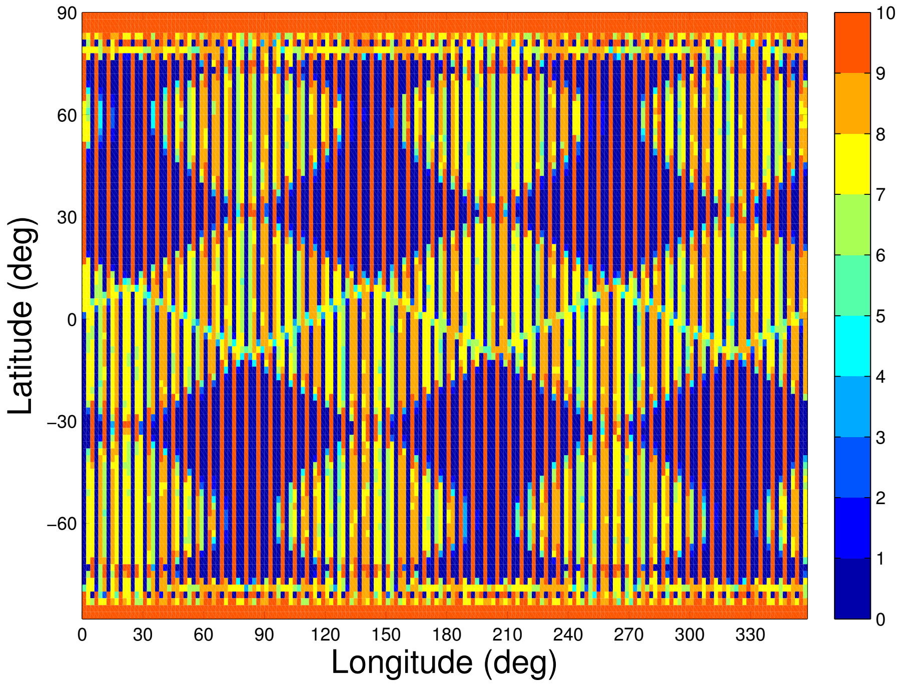

Figure 4.4: Number of passes through 2° × 2° bins during September 2004.

The plot resulting from grouping the observations into smaller bins looks similar to that in which the bins were 3° on each side. However, significantly fewer of these smaller bins were actually passed over in relation to the total number available (62.2% as opposed to 78.7%). For comparison, the period of uniform coverage during February had passes through 100% of the bins for both bin sizes. The even lower percentage of smaller bins passed through indicates that the repeat ground track does a worse job of recovering a 90×90 field, as shown in Chapter 3.

To illustrate this point further, the coverage during the 107/7 repeat period is also examined. When allocating the passes according to 3° bins, the lack of spatial coverage during this longer repeat period appears to be somewhat less profound, as seen in Figure 4.5.

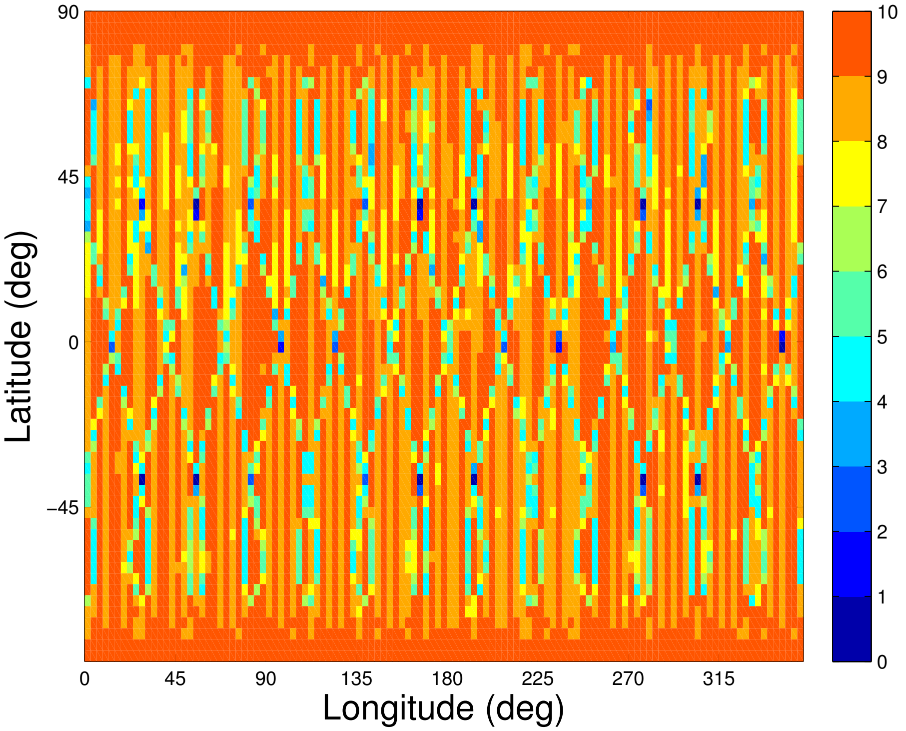

Figure 4.5: Number of passes through 3° × 3° bins during December 2009.

Figure 4.5 shows that nearly all of the bins are passed through at least once during the course of the month-long data span (99.8%). However, since the observability of a gravity field with $L_{MAX} = 60$ is represented by a study with this bin size, this shows that even a repeat configuration with 107 revolutions does not entirely cover every region necessary for a perfect recovery.

The onset of anomalistic singular values around this field size (as seen in Figure 3.17) reinforces the notion that the solution is experiencing a minor form of degradation at this stage. When 2° × 2° bins are used in Figure 4.6, the reduced coverage becomes more apparent.

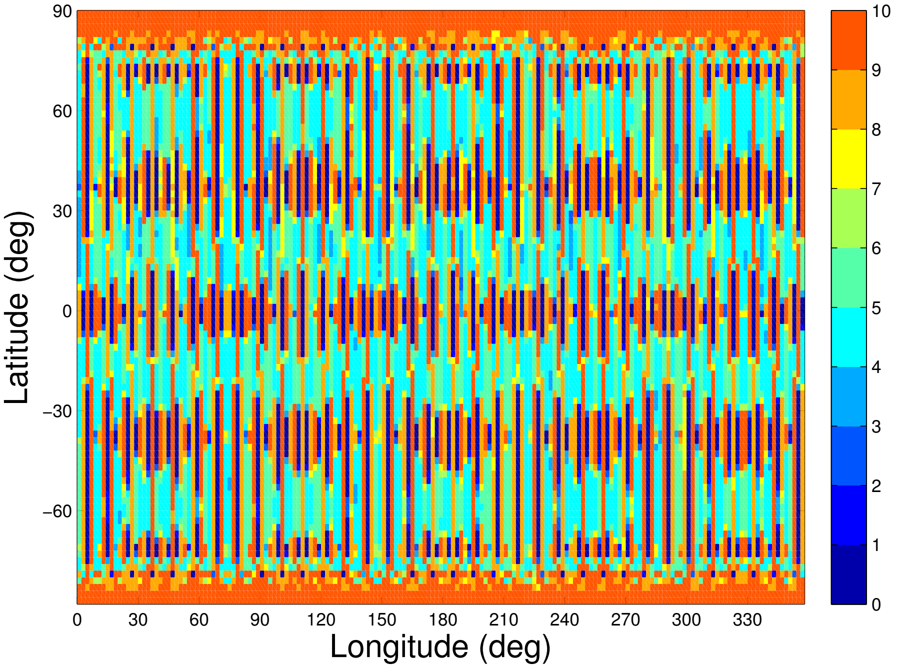

Figure 4.6: Number of passes through 2° × 2° bins during December 2009.

There is now a greater percentage of bins that are unfilled (87.8% full), but the coverage still remains fairly adequate. Recall that the major portion of degradation occurs when $L_{MAX} = R$. This means that a 90 × 90 field can still be resolved fairly well, but with higher uncertainty than the smaller fields (including the degree and order 60 field addressed earlier). There appears to be a threshold at which the percentage of bins passed through relates to the point at which degradation occurs. The onset of minor degradation seems to start as soon as 100% coverage is no longer achieved and the major degradation phase could appear as soon as the coverage drops to about 85%.

This study helps to envision the link between spatial coverage and gravity field fidelity from a geometric standpoint. When the desired gravity solution size grows, there must be observations of the nonspherical perturbations at a finer resolution or else there will be insufficient information to fully recover the field. To build upon this study, a simple simulation is conducted in the following section.

4.2 Simulation of Degradation Effects

The previous section showed the dispersion of GRACE observations over the surface of the Earth during uniform coverage and repeat ground tracks. Furthermore, a rough requirement for observation resolution was imposed in the form of dividing the Earth's nonspherical gravitational influence into "bins" and collecting satellite passes. However, the study dealt purely with the geometry of the passes and not with the quantitative effect on resolving the harmonic coefficients.

In order to determine these consequences, a simulation is set up to mimic the observations of the Earth's geopotential that a hypothetical GRACE mission would experience in the two different ground track layouts and calculate the resulting gravity fields. To form a baseline, both scenarios use the same Earth gravity model to represent the field that they are observing and trying to recreate as accurately as possible. The surface of the Earth is then divided into equally sized bins as with the study in the previous section. To represent the case where GRACE provides uniform coverage of the Earth, the derivative of the "up" component of the gravitational potential is calculated analytically at the location of the center of each bin. The degraded case only generates observations at the centers of bins that are passed over during the repeat period of September 2004. Using the resulting series of simulated observations, each scenario re-estimates the harmonic coefficients to determine how well the original gravity field was able to be recovered when provided with the corresponding spatial coverage.

The degree difference variance (DDV) is an ideal statistic to quantify the differences between the original and re-estimated fields because it directly compares the harmonic coefficients, rather than their uncertainties. For this simulation, the grid was chosen to be finer than in the studies conducted in Section 4.1 ($1^\circ \times 1^\circ$ bins).

These smaller bins were chosen to ensure that "stable" solutions were obtained during the re-estimation process with the field sizes that are being analyzed. Equation 4.1 serves as somewhat of a criterion to establish the relationship between solution size and spatial resolution. This can be thought of as analogous to the Nyquist frequency associated with sampling a time series. For a given field size to be solved for, $\Delta\lambda$ defines the absolute maximum size of a grid that must be fully occupied to recover the field. In practice, over-sampling is desired to ensure a sufficient amount of data and usually provides a better solution. For example, "uniform" data sets that consist of observations at differing resolutions can lead to a variety of results. This is illustrated in Figure 4.7, where reconstructed fields are produced using data originating from different grid sizes.

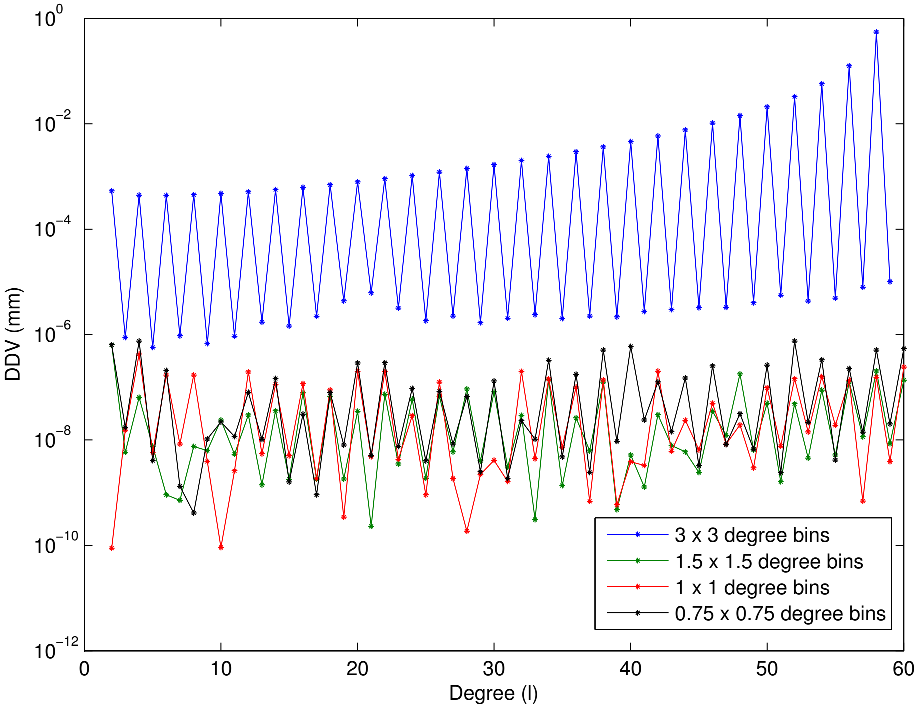

Figure 4.7: Degree difference variance between the original gravity field and the re-estimated solution using uniform measurements with different bin sizes.

All of the fields in Figure 4.7 were recovered to $L_{MAX} = 60$, so the blue plot arising from a $3° \times 3°$ field is similar to the scenario depicted in Figure 4.2, although the simulation contains only one measurement in each bin. Despite uniform coverage from all four cases, the blue plot corresponding to the lowest observation resolution produces a field that is several orders of magnitude worse in terms of DDV than its counterparts. The higher DDV values indicate that the original field is not as accurately reproduced by the estimation process given the available data. At a certain point, the size of the bins no longer affects the quality of the solution and stability is said to have been achieved. Therefore, a $1^\circ \times 1^\circ$ grid was chosen for the simulation because it was a whole number that was sufficiently well-behaved. With the proper grid size established, a comparison could be made between this uniform coverage and the layout represented by the 61/4 repeat ground track. The statistics associated with the resulting fields are depicted below in Figure 4.8.

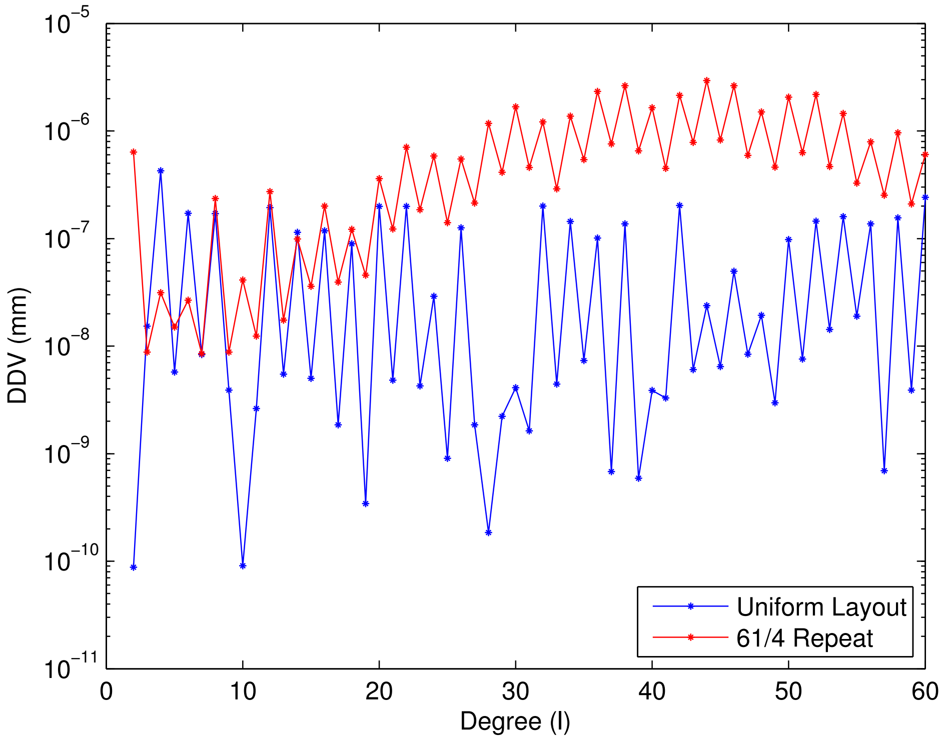

Figure 4.8: Degree difference variance between the original gravity field and the re-estimated solution for a 60×60 gravity field.

Figure 4.8 shows that the DDV is lower at most degrees when uniform coverage is provided, meaning the original field was more accurately recreated. It is worthwhile to note that these results are entirely in the absence of noise, so this study serves as a good means to qualitatively compare the various solutions. Recall from the previous section that the onset of major degradation was seen when only 85% of the total number of bins were occupied. With this spatial resolution, only 40.0% coverage is achieved during the 61/4 repeat ground track, so the reconstructed field is highly degraded. In particular, the

DDV values beyond degree 20 were two to three orders of magnitude higher when there was a reduction in coverage.

The difference in solution quality between the uniform and repeat ground tracks for a fixed solution size has been well documented thus far. Another important aspect of gravity recovery during repeat ground tracks is the dependency of solution accuracy on the size of the field. To do this, the same repeat layout was used to reproduce an original field of different sizes. The DDV plots associated with these solutions are shown in Figure 4.9.

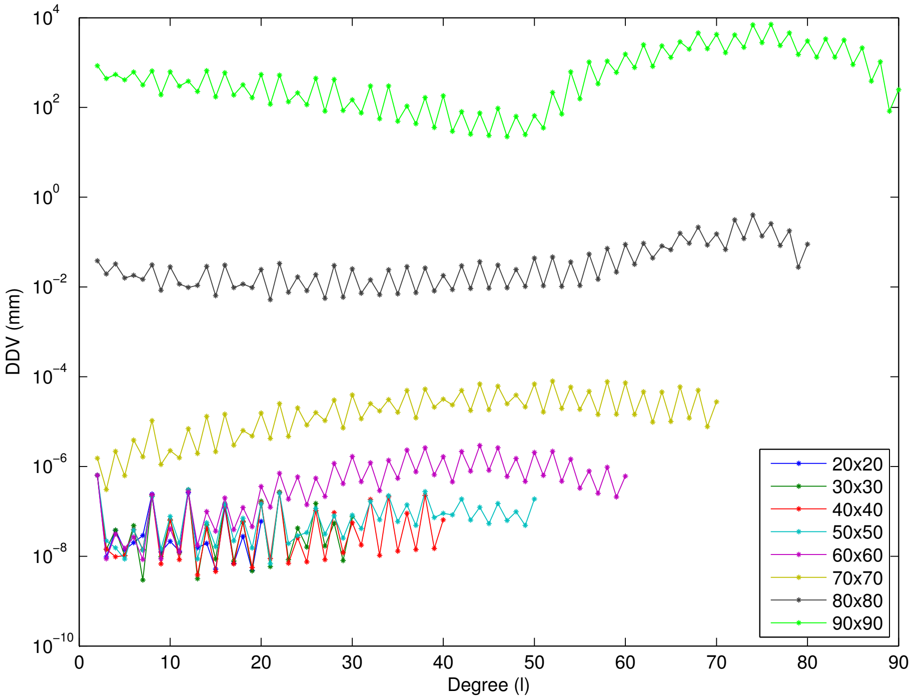

Figure 4.9: Degree difference variance between the original gravity field and the re-estimated solution produced by the simulation using the 61/4 repeat ground track.

The shape of these plots show similar overall behavior to the DEV plots in Figure 3.4b in that the results between the field sizes of $L_{MAX} = 20$ and 60 closely resemble each other. Beyond these fields, the DDV increases drastically for each subsequent solution, which is further confirmation of the effects of major degradation and the field size at which it occurs. The minor degradation phase is visible to a lesser extent, with the DDV increasing gradually between the 30×30 and 60×60 fields.

This study has effectively shown how the lack of spatial coverage can influence the ability to recover a gravity field by constructing a situation in which a known baseline field can be re-estimated. In addition, there was no noise involved in the simulation, so the effects of coverage could be further isolated. Ultimately, trends were seen that were similar to those encountered with actual GRACE data, reinforcing the concept of two phases of degradation occurring in the presence of a repeat ground track. With the interaction between spatial coverage and solution quality addressed, the role of perturbation frequencies will be further explored.

4.3 The Effect of Gravity Field Size on the Resulting Perturbation Frequencies

The solution degradation that occurs during repeat periods can also be analyzed from the standpoint of the perturbation frequencies associated with the estimated harmonic coefficients. As mentioned in Chapter 2, when a repeat ground track is encountered, the unique perturbation frequencies start to become duplicated by higher coefficients in the gravity field. The overall "aliasing" effect of this phenomenon is observed when the mathematical process behind the estimation of harmonic coefficients is examined.

The estimation problem involving the harmonic coefficients is well-defined as long as there are more unique perturbation frequencies than coefficients to be estimated. In a month where there is uniform coverage, there are many more perturbation frequencies than coefficient estimates, so a relatively large gravity field can be adequately determined. However, when higher degree and order coefficients no longer produce unique perturbation frequencies (as with the repeat period), a field size is encountered that contains more unknown coefficients than unique frequencies. The previously well-determined estimation problem becomes underdetermined, leading to an increase in uncertainty of the gravity solution. The field size at which duplicate frequencies start to arise is dependent on the wave number N and ultimately the number of revolutions and days that characterize the particular repeat period. Figure 4.10 provides a graphical representation of the numbers of unique perturbation frequencies and unknown harmonic coefficients to be solved for as the field size grows.

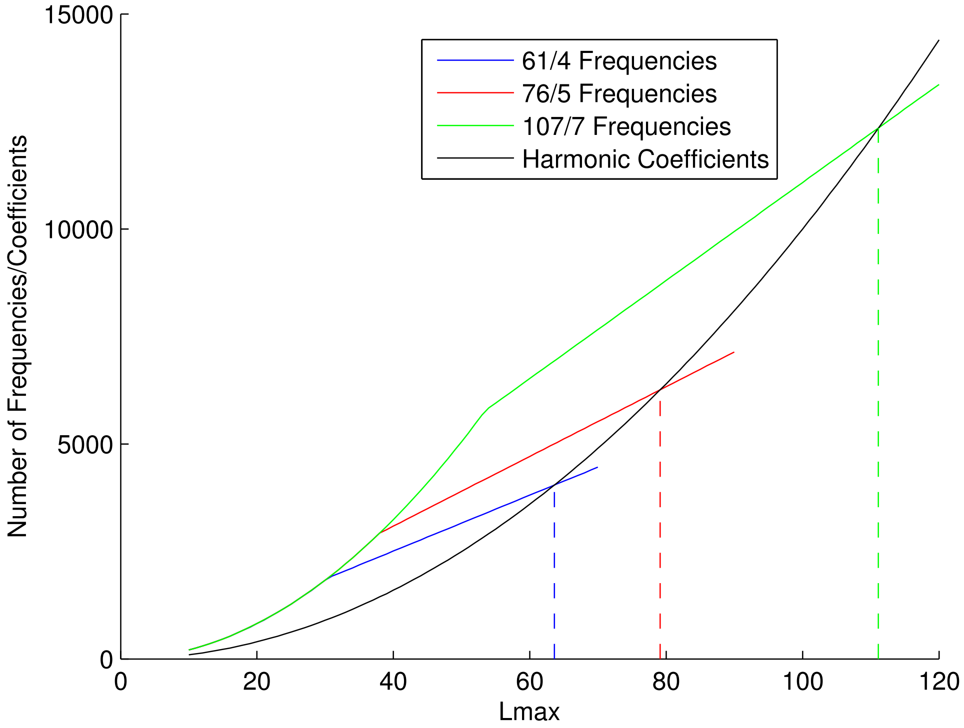

Figure 4.10: Number of unique perturbation frequencies and estimated harmonic coefficients for various repeat periods.

It can be seen from Figure 4.10 that the number of unique frequencies follows the same nonlinear trend for every repeat period up to a certain point. During a period of ideal global coverage, this trend would continue upwards, meaning that there will always be enough information to determine the gravity field. However, at a certain point, the signal strength from extremely high degree and order harmonics becomes dominated by measurement noise and these harmonics cannot be resolved.

For the repeat scenarios, this behavior deviates to a slower increase at $L_{MAX} = \frac{R}{2}$. This corresponds to where the solutions experience the minor first phase of solution degradation. At this point, many of the harmonics introduced with an increase in field size will have an opposite perturbation frequency of a set of harmonics already existing in the smaller fields. The Colombo-Nyquist rule dictates that unique frequencies (and their associated wave numbers) must not be the same magnitude, so these new coefficients are now aliased with many of the existing ones. However, the number of unique frequencies still rises linearly because many of the highest degree and order coefficients that are introduced possess frequencies that are also unique.

The number of harmonic coefficients for a given field size follows a distinct pattern ($[L_{MAX} + 1]^2 - 4$). Since the rate at which unique frequencies are introduced is reduced beyond $L_{MAX} = \frac{R}{2}$, there is a threshold beyond which all field sizes will contain more unresolved harmonic coefficients than frequencies for every repeat period. Upon further inspection, this threshold is located at roughly $L_{MAX} = R$, which is the point at which major degradation occurs. A useful way to represent this relationship is to observe the ratio of the unique frequencies to estimated harmonic coefficients. These plots appear in Figure 4.11.

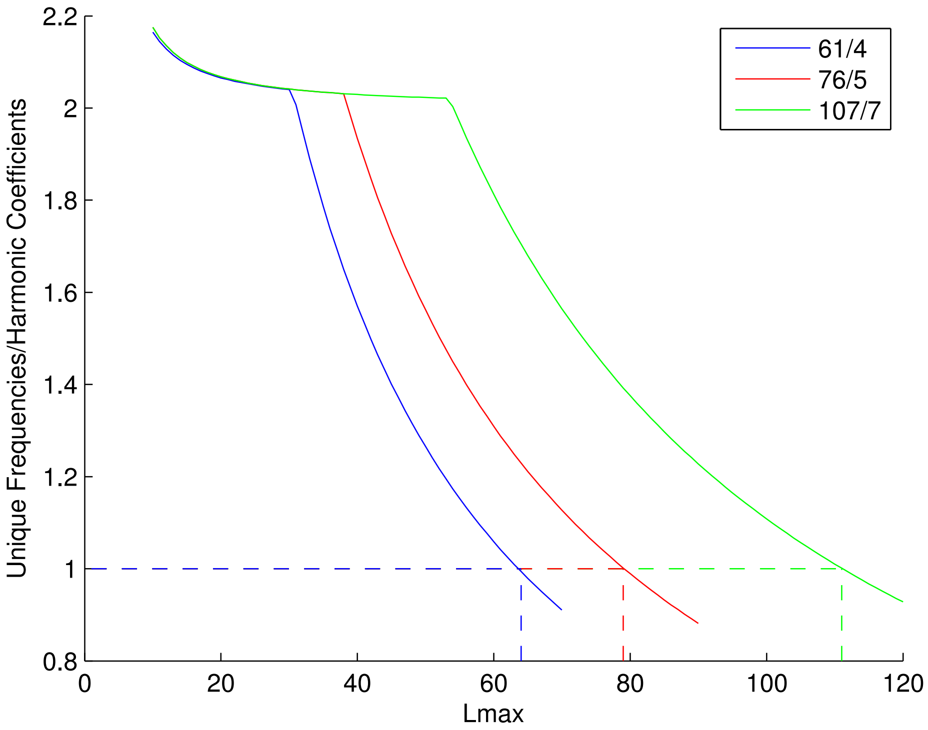

Figure 4.11: Ratio of unique perturbation frequencies to harmonic coefficients for various field sizes.

This visualization helps to confirm the conclusions reached in Figure 4.10. The ratio of unique frequencies to harmonic coefficients appears to asymptotically approach 2, indicating that the system is well-defined in those scenarios. However, the reduced rate at which unique frequencies are generated near $L_{MAX} = \frac{R}{2}$ causes the ratio to sharply decline. Since the estimation problem involving the determination of harmonic coefficients is no longer well-defined once there are fewer unique frequencies than harmonic coefficients, this threshold is represented by a ratio of 1. Beyond this point, which is roughly near $L_{MAX} = R$, a significant loss of information occurs and the quality of the solution greatly suffers. The minor degradation phase corresponds to the field sizes where the ratio is decreasing, but still above unity. The slight loss of information has an adverse effect on the resulting solutions (as shown in Chapter 3), but the increase in uncertainty is not overwhelming when compared to the calibrated error levels, as shown in the following section.

4.4 Relation to Calibrated Error Estimates

As mentioned in Chapter 2, the formal sigmas that are used to calculate the degree error variances throughout this thesis are just one of the products delivered by the GRACE science team. A different representation of the uncertainties, known as calibrated error estimates, are often preferred by the science community because they are more realistic. Since the calibrated errors take the place of the formal sigmas, degree error variances can be calculated in the same fashion. By comparing these degree error variances with those appearing in the earlier analysis, a sense of perspective can be established on the significance of the observed levels of degradation.

As with the formal sigmas, one set of calibrated error estimates are delivered per monthly solution. However, they are only generated up to degree and order 60 since this range covers most of the time-varying portion of the field. Regardless, general trends can still be inferred from relatively limited information across the spectrum of field sizes. As mentioned in Chapter 2, the error values used for this analysis are taken from RL04 data and adjusted by a factor of $\frac{1}{\sqrt{2}}$ to represent the anticipated calibrated errors that will be seen in the upcoming RL05 series. The formal degree error variances for various field sizes are plotted along with the calibrated degree error variances for the ideal month of February 2004 in Figure 4.12.

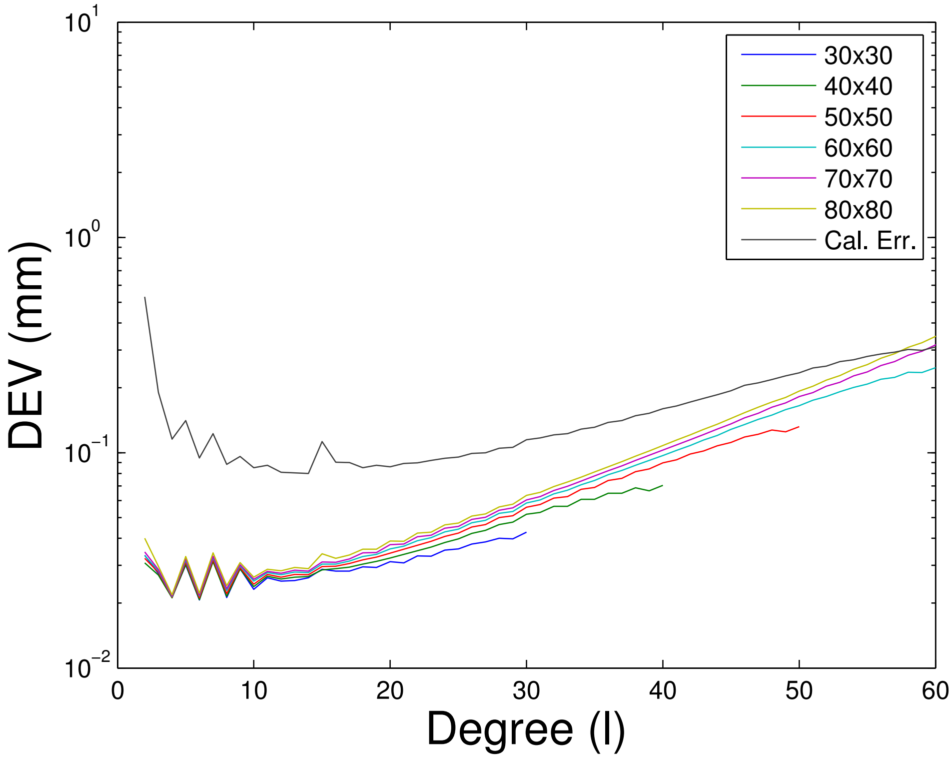

Figure 4.12: Comparison of calibrated error estimate and formal sigma degree error variances for February 2004.

Figure 4.12 confirms that the calibrated errors are a more conservative representation of the gravity field because the uncertainties are roughly an order of magnitude higher across most of the degrees. It should be noted that a few of the degrees close to 60 have lower calibrated error values than formal sigmas. This is an artifact of the calibrated errors only existing to $L_{MAX} = 60$, since the two gravity solutions that have certain higher DEV values have a larger L_{MAX}. If the calibrated errors were generated for larger fields, the DEV would be higher because the lower degrees would be corrupted by the higher uncertainties corresponding to the new higher degrees. This effect is demonstrated by the gradual increase in DEV at all degrees as the field size grows, but the magnitude of the increase in uncertainty is generally lower than the calibrated error level, meaning that it is relatively benign. However, when the two forms of DEV are compared during the 61/4 repeat period, as in Figure 4.13, a different pattern emerges.

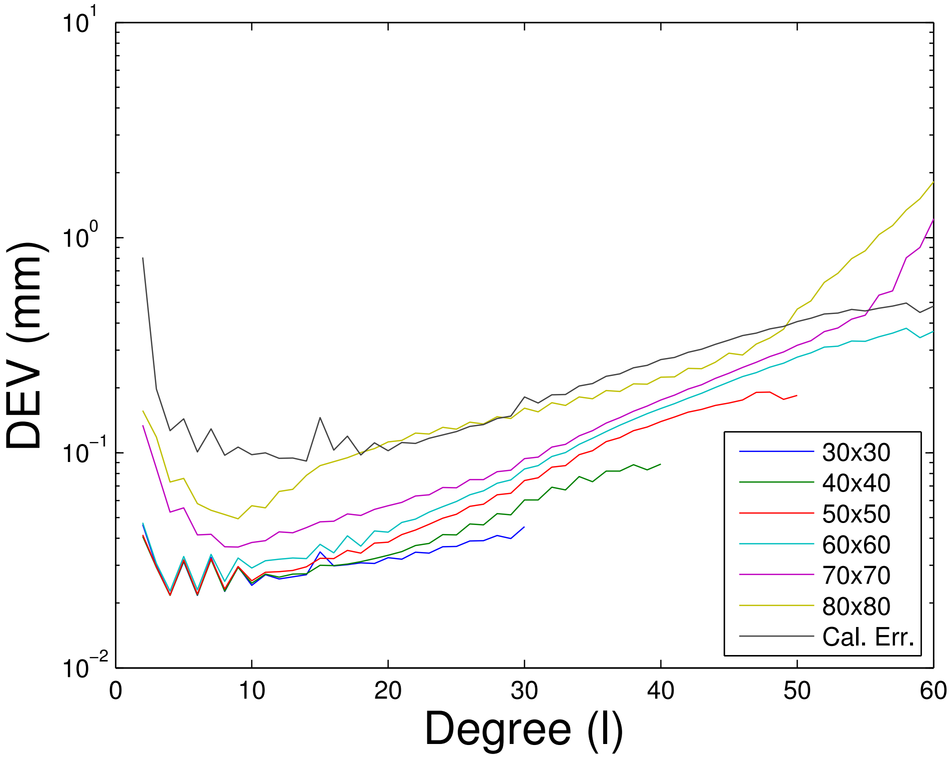

Figure 4.13: Comparison of calibrated error estimate and formal sigma degree error variances for September 2004.

Upon inspection, the calibrated error levels are still higher than the formal ones for a majority of the field sizes, but unsurprisingly, when the transition is made across the threshold of major degradation, there are certain formal errors that surpass the calibrated ones. This indicates that the error levels corresponding to major degradation are significant because they are above those released by the GRACE team that are supposed to account for additional unmodeled effects. However, the field sizes affected by minor degradation (between $L_{MAX} = 30$ and 60 in this case), are still well below the calibrated error levels. Although a rise in uncertainty is seen in these field sizes during a repeat period (as seen in Figure 3.5), the extent of the degradation is insignificant relative to the other error sources influencing the gravity solution.

Even when the conditions are such that a solution experiences major degradation that results in uncertainties above the calibrated error levels, a solution is nonetheless obtained. This is somewhat inconsistent with what the Colombo-Nyquist rule predicts. An important caveat of the Colombo-Nyquist rule is that its consequences are only valid during exact repeat conditions. When GRACE passes through a repeat period, it only experiences the combinations of orbital elements required for an exact repeat ground track at an instantaneous point in time. Since the gravity solutions produced from GRACE data contain observations from an entire month, there is a substantial amount of time that GRACE does not fulfill this "requirement". Therefore, for a month such as September 2004 containing a sparse ground track, GRACE is only said to exhibit near-repeat conditions. However, the perturbation frequencies associated with the lumped harmonics while GRACE is in near-repeat conditions are still very similar. This results in only a weak observation of the harmonic coefficients outside of what is predicted by the Colombo-Nyquist rule, but they are still able to be determined (with less certainty).

Another important assumpton that is made by the Colombo-Nyquist rule (and in Chapter 2 of this thesis) is that the sideband perturbation frequencies were considered to be negligible. In the full expression for the perturbation frequency associated with a lumped harmonic set (Equation 2.7), there was a term involving the index q that was assumed to be zero. This assumption was made to simplify the analysis and is reasonable given the GRACE orbit's low eccentricity. However, eliminating this term neglected infinitely many sideband frequencies that are acting on the satellite, although their effects are relatively small. Regardless of the low "power" of the signal coming from these sideband frequencies, they provide more unique frequencies to make the estimation problem more well-conditioned in cases where there are originally too many unknown harmonic coefficients.

During the latter portion of the writing of this thesis, a study was published that revisited the Colombo-Nyquist rule and reached many of the same conclusions as were stated in the paragraphs above [29]. This analysis was conducted using simulated data for a variety of measurement types, including the low-low satellite observations that are central to GRACE mission. The processing technique was similar to that used for the generation of GRACE gravity solutions in that a weighted least squares solution was estimated using measurement partials. This study helped to confirm one of the primary conclusions of this thesis, which is that there are two phases of solution degradation dependent on the number of revolutions in the repeat period. This discovery led to the recommendation that the Colombo-Nyquist rule is incomplete and needs to be reformulated.

However, there are certain disparities that exist between the study and the results and subsequent conclusions presented in this thesis. Although two phases of degradation are identified by the paper, the authors observe that the maximum obtainable field size is dependent on the type of measurement being taken. For example, the study claims that low-low observations are sufficient to recover a field that is twice as large as what this thesis concludes ($L_{MAX} = 2R$) [29]. In addition, the authors suggest that combining measurement types (such as augmenting the low-low observations with GPS data) will increase the maximum resolvable field size even further. Considering that GRACE also utilizes GPS measurements for precise orbit determination, there appears to be an inconsistency in the increase in performance that is predicted.

The generally optimistic results reported by this study could potentially arise from certain aspects of the procedure and some of the underlying assumptions that were made. For example, the nature of the study eliminated any errors of omission that caused the lower degree and order coefficients to become contaminated by the larger ones during situations where degradation was present. Also, the study simulated inter-satellite measurements that were sampled more frequently and of higher precision than what GRACE records. This paper was published too late into the analysis that went into this thesis to examine the discrepancies in much detail, but resolving the apparent inconsistencies would be a worthwhile endeavor. Regardless, the study helps to reinforce the notion that the Colombo-Nyquist rule is not complete.

This chapter has examined a variety of the fundamental consequences of determining a gravity field using data from periods of reduced spatial coverage. First, this problem is approached in terms of the geometry of the ground track. The portions of the Earth that should be observed by GRACE to declare adequate coverage can be envisioned by dividing the surface of the Earth into equally sized cells. The size of these cells is inversely proportional to the fidelity of the desired gravity field, with larger field sizes leading to a smaller grid (and therefore more cells that need to be occupied). It is shown that a month containing uniform coverage has several passes through each portion of the grid, indicating that the nonspherical gravitational influence has been adequately encountered and captured in the resulting data set. However, the months containing repeat periods have stripes of unobserved areas if the cells are too small. This reinforces the notion that large gravity solutions will be inaccurate during these times because GRACE does not experience the full effect of these perturbations.

The relationship between the number of unique perturbation frequencies and estimated harmonic coefficients for a given field size is also addressed. This can be linked to the estimation problem that is used to obtain solutions for the harmonic coefficients from the measurements that GRACE collects. When there are fewer unique perturbation frequencies than coefficients to be estimated, as in the case of major degradation, the estimation problem suffers from a lack of observability.

This can be explained by revisiting the information matrix $\boldsymbol{H}$. Simply put, it contains the relationships between the parameters being estimated and the expected observation values. During resonance, multiple lumped harmonic sets can represent a particular perturbation frequency so that the list of observations cannot distinguish between the two sets, an effect similar to aliasing. In terms of the estimation problem, this phenomenon will cause linearly dependent columns to appear in $\boldsymbol{H}$ where these redundancies occur and $\boldsymbol{H}^T\boldsymbol{W}\boldsymbol{H}$ will no longer be full rank. Although the processing of GRACE data does not involve the inversion of $\boldsymbol{H}^T\boldsymbol{W}\boldsymbol{H}$, the properties of $\boldsymbol{H}$ have a direct effect on the conditioning of the $\boldsymbol{R}$ matrix in QR factorization.

In theory, a matrix that is not full rank will have a singular value of zero for every linearly dependent row/column. The situation that would lead to linearly dependent columns corresponds to a time when the exact repeat conditions are met. However, Figure 3.18 shows that the lowest singular values seen during the solution spanning the month of September 2004 are on the order of 10^2 for a 120×120 field. This is likely due to the inclusion of observations from the days surrounding the exact repeat conditions, where the previously identical perturbation frequencies of certain lumped harmonic sets show some disparity. This has the effect of making some of the columns of $\boldsymbol{H}$ only *nearly* linearly dependent, rather than totally linearly dependent. While still not a desirable problem from a computational standpoint, a solution can be obtained but at the cost of increased uncertainty (as shown in the DEV plots).

Recall that these detrimental effects involving the occupation of identical perturbation frequencies only apply when the field size is large enough to allow for such behavior. Generally speaking, when GRACE passes through a repeat period, the problem could become much less observable if the field size in the solution is too large.

Chapter 5

Conclusions and Recommendations for Future Work

Analysis of GRACE gravity solutions and their associated statistics for a variety of field sizes and repeat ground track conditions has provided evidence that there are two phases of solution degradation that occur when the estimated field size is large enough. This conclusion was reached by examining the behavior of the degree error variance plots and singular values associated with the various solutions. The onset of these two phases is dependent on the severity, or lack of spatial coverage, associated with the particular ground track.

In particular, the gravity solution will experience minor degradation at fields that are roughly $L_{MAX} = \frac{R}{2}$ and larger, where R is the number of revolutions of the satellite in the repeat cycle. The minor degradation consists of a noticeably higher uncertainty in the middle to high degrees of the gravity solution, but the increase in uncertainty is insignificant compared to the calibrated error statistics. When field sizes larger than $L_{MAX} = R$ are estimated, the solution is subjected to major degradation, where the underlying estimation problem becomes numerically ill-conditioned from a computational standpoint. This phenomenon is demonstrated by examining the singular values and resulting condition numbers of both well-behaved and ill-conditioned scenarios.

The onset of major degradation is linked to a lack of spatial coverage in the data span used for the particular solution. In such a case, columns of the $\boldsymbol{H}$ matrix become nearly linearly dependent, which has an adverse effect on the numerical conditioning of the estimation problem. This can ultimately be viewed as a significant decrease in observability of the unknown harmonic coefficients of interest. Although GRACE processing uses QR factorization, the properties of $\boldsymbol{H}$ have a direct relationship to the $\boldsymbol{R}$ matrix that is utilized instead.

The two phases of degradation are also intimately tied to the ratio of unique perturbation frequencies to the number of unknown harmonic coefficients. The number of harmonic coefficients to be estimated increases quadratically with L_{MAX}, but the number of unique perturbation frequencies is dependent on the wave number N associated with the repeat ground track that occurs during the data span. The wave number is directly linked to the number of orbital revolutions R in the repeat cycle, so a relationship exists between R and the ratio of unique frequencies to harmonic coefficients.

The number of unique frequencies rises quadratically until the field size reaches roughly $L_{MAX} = \frac{R}{2}$, which is found to be the threshold of minor degradation. Beyond this point, the number of unique frequencies increases linearly, but the ratio begins to drop. When the number of coefficients to be solved for is equivalent to the number of unique frequencies, solutions begin to experience major degradation due to a breakdown in the underlying estimation problem. This occurs at roughly $L_{MAX} = R$, which is consistent with the results that were observed in the degree error variance and singular value plots.

These findings conclude that the Colombo-Nyquist rule is incomplete. It predicts that solutions will experience the effects associated with major degradation at field sizes corresponding to the earlier minor phase, which is $L_{MAX} = \frac{R}{2}$. Solutions beyond $L_{MAX} = \frac{R}{2}$ are of only slightly reduced quality and still considered to be useful. In fact, the major form of degradation postulated by the Colombo-Nyquist rule occurs at twice the field size ($L_{MAX} = R$). The rule itself is mathematically sound, but there are many assumptions being made in its formulation that cause it to break down when assessing GRACE gravity solutions.

As mentioned in Chapter 4, a paper was published during the final stages of this thesis that addressed similar topics. Many conclusions were made which supported those made in this thesis, but there were also several inconsistencies that could not be investigated due to lack of time. Primarily, the study predicted that a satellite mission with an instrument suite comparable to GRACE could recover larger gravity fields than this thesis has concluded without the aid of *a priori* information or regularization. Determining the source of this discrepancy is a highly important task. Also, the study examines interesting aspects of solution degradation that were not considered as part of this analysis, such the RMS values of uncertainty as a function of geographic location. Another opportunity for analysis involves identifying how the behavior varies depending on the mathematical parity of R and D.

Also mentioned as part of the underlying theory was an assumption made to neglect the sideband gravitational perturbation frequencies acting on GRACE because of its orbital eccentricity being nearly zero. This choice was made because the formulation of the Colombo-Nyquist rule was founded upon the same assumption. Since the effects of the sideband frequencies are fairly small relative to those that were used in this thesis (corresponding to $q = 0$), this assumption was reasonable to make in order to simplify the analysis. However, this assumption is possibly one of the biggest pitfalls of the Colombo-Nyquist rule's prediction. Accounting for sideband effects introduces many more unique perturbation frequencies into the estimation problem and could be another underlying reason why GRACE is still able to obtain reasonable gravity fields during repeat periods at field sizes larger than what the Colombo-Nyquist rule dictates. However, the relative strength of these sideband effects and how much of a role they play in aiding the recovery of gravity fields during these periods is not very well known. Expanding upon the analysis done in this thesis to quantify these contributions and identify their significance could be useful in establishing a holistic understanding of the problem.

Another point of interest is that GRACE was in the process of passing through a 3-day repeat cycle consisting of 46 orbital revolutions at the time this thesis was written. This is the worst spatial coverage that GRACE has provided throughout its lifetime. In theory, this should also produce the worst gravity solutions because of the low observability. This thesis only examined three different repeat periods, and generalizations were made based upon the behavior of the gravity solutions during these spans. A fourth set of solutions, especially ones that are anticipated to see the most degradation, will help to validate the conclusions made in this study.

The calibrated error estimates that accompany the formal GRACE coefficient solutions were included to serve as a baseline for comparison. The level of the calibrated errors was high enough such that it made the uncertainty increase associated with minor degradation insignificant. As mentioned previously, the calibrated error estimates are linked to the quality of the data and how accurate the model is. Future geodetic satellites, such as the GRACE Follow-On mission, might achieve data accuracies that lead to substantially lower calibrated error estimates. This could cause the disparity between the formal and calibrated sigmas to vanish, making the minor degradation phase lead to a significant adverse effect in solution quality. If a geodetic mission is launched in the future with the ability to make this possible, similar analysis to what was performed in this thesis would be worthwhile in order to more accurately assess the ramifications of the Colombo-Nyquist rule.

Appendices

Appendix A

Representation of the Earth's Gravity Field

The Earth's gravity field is most commonly expressed in terms of the gravitational potential U. The potential associated with a uniform density spherical body (which can be approximated as a point at the center of mass) is well known to be:

$$U = \frac{\mu}{r} \tag{A.1}$$

where μ is the gravitational parameter of the body and r is the distance of the satellite from the center of the body. Using this approximation for the gravitational potential of the Earth results in Keplerian motion of the satellite, which is a reasonable depiction of reality. However, a more accurate representation of the various forces on the satellite are usually required for actual missions. There are many different sources that contribute to a deviation from Keplerian motion (known as perturbations), such as a non-spherical Earth, third-body effects, and solar radiation pressure [27]. The effects that are deemed to be relevant depend on the geometry of the orbit, among other things.

This thesis is concerned with the largest source of perturbations for GRACE, which is the non-sphericity of the Earth. In this case, the potential function is split into the contributions from the spherical and non-spherical portions of the Earth. The potential function can now be expressed as:

$$U = U_{2-body} + U_{NS} \tag{A.2}$$

As mentioned before, the 2-body portion of the potential function is well known. Because of this, the accuracy of the potential function in this formulation is directly dependent on the ability to provide a good model for the non-spherical characteristics of the Earth. The most common way to characterize the deviations associated with the Earth involves the use of spherical harmonics.

Spherical harmonic coefficients are used to describe the mass properties of the Earth in general, particularly the mass distribution. A set of harmonic coefficients become a way to represent the shape, and resulting gravity field, of the Earth. The coefficients consist of a cosine and sine component (C_{lm} and S_{lm})for a given degree l and order m. As the degree and order get higher, the coefficients correspond to variations in the Earth at a finer resolution.

The harmonic coefficients can be visualized on the surface of a sphere by their nodal lines, or places where the value on the sphere is zero. This corresponds to a root of the associated Legendre polynomial, which will be introduced shortly. The harmonics that have order $m = 0$ are purely a function of the latitude of the sphere and are known as zonal harmonics. The coefficients that have the same degree and order ($l = m$), called sectorial harmonics are strictly longitude dependent. All of the other terms that have nonzero degree and order that are not equal to each other can be represented as a combination of the zonal and sectorial harmonics. The result is a separation of the surface of the Earth into tile-shaped portions, resulting in the classification as tesseral harmonics. A visual is provided below which illustrates the different classifications just described:

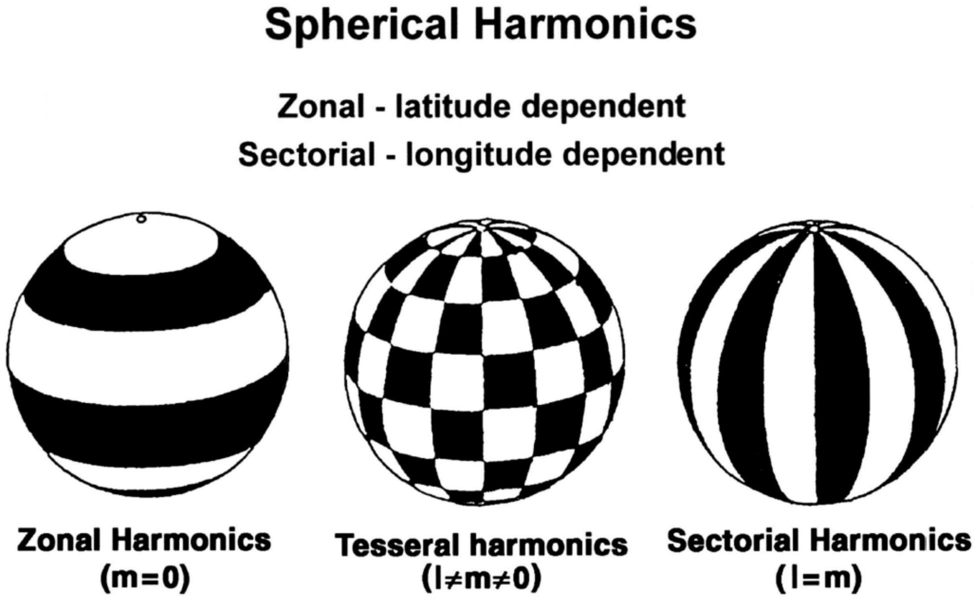

Figure A.1: Spatial representation of the different types of Earth's spherical harmonics.

The values of the conventional harmonic coefficients at higher degree and order become very small, which can pose a problem in terms of computation [27]. Therefore, the use of normalized coefficients has become the standard in the field of geodesy. The conversion between conventional and normalized spherical harmonics is achieved via the following relationships:

$$\begin{aligned} \overline{C}_{lm} &= K_{lm} C_{lm} \\ \overline{S}_{lm} &= K_{lm} S_{lm} \end{aligned} \tag{A.3}$$

where

$$K_{lm} = \sqrt{\frac{(l+m)!}{(2-\delta_{0,m})(2l+1)(l-m)!}} \tag{A.4}$$

and $\delta_{0,m}$ is the Kronecker delta, which is 1 when $m = 0$ and 0 when $m \neq 0$. To define the origin of the Earth to be at its center of mass, the harmonic coefficients $\overline{C}_{1,0}$, $\overline{C}_{1,1}$, and $\overline{S}_{1,1}$ are set to zero [21]. With the help of normalized harmonic coefficients, the non-spherical contribution of the Earth's scalar potential can now be expressed as

$$U_{NS} = \frac{\mu}{r} \sum_{l=2}^{\infty} \sum_{m=0}^{l} \left(\frac{a_e}{r}\right)^l \overline{P}_{lm} (\sin \phi) \left[\overline{C}_{lm} \cos (m\lambda) + \overline{S}_{lm} \sin (m\lambda)\right] \tag{A.5}$$

where a_e represents the Earth's equatorial radius, ϕ is the geocentric latitude of the satellite, and λ is the longitude. Also, $\overline{P}_{lm}$ is the normalized associated Legendre function evaluated for degree l and order m of the expansion. Since Equation A.5 provides the potential function in terms of spherical coordinates (r,ϕ,λ), the resulting potential field is expressed in a body-fixed reference frame. An alternate formulation can be obtained using linear perturbation theory that represents the scalar potential in relation to the Keplerian elements of the satellite's orbit [10]:

$$U_{NS} = \sum_{l=2}^{\infty} \sum_{m=0}^{l} \sum_{p=0}^{l} \sum_{q=-\infty}^{+\infty} \frac{\mu}{a} \left(\frac{a_e}{a}\right)^l F_{lmp}\left(i\right) G_{lpq}\left(e\right) S_{lmpq} \tag{A.6}$$

where the parameter r has been replaced with the semi-major axis a and F_{lmp} and G_{lpq} are functions of the inclination i and eccentricity e of the orbit [10]. Also, $-\infty \leq q \leq \infty$ and $0 \leq p \leq l$. The term S_{lmpq} takes the form:

$$S_{lmpq} = \begin{bmatrix} C_{lm} \\ -S_{lm} \end{bmatrix} \cos\psi_{lmpq} + \begin{bmatrix} S_{lm} \\ C_{lm} \end{bmatrix} \sin\psi_{lmpq} \tag{A.7}$$

where the upper term in the brackets is used when $l-m$ is even and the lower term is used when $l-m$ is odd. The angular term, which is sometimes referred to as the Kaula gravitational argument [27] is

$$\psi_{lmpq} = (l-2p+q)M + (l-2p)\omega + m(\Omega - \theta_e) \tag{A.8}$$

where ω, M, and Ω are the classical Keplerian elements and θ_e is the Greenwich hour angle [1].

The quadruple sum listed in Equation A.6 is a convenient way of showing how the potential function varies according to the geometry of the orbit. It is also in the form that is compatible with Lagrange's Planetary Equations to determine the time derivatives of the Keplerian elements due to non-spherical perturbations. Expanding the sum to include higher degree and order terms will result in a gravity field model with finer spatial resolution and will presumably be a more accurate representation of reality. This requires a knowledge of the harmonic coefficients to the desired degree and order, so much effort has been devoted by the scientific community to accurately determining them.

Appendix B

Estimation Theory

GRACE data processing incorporates the batch filtering technique to estimate the parameters of interest. One of the fundamental attributes of batch processing (as opposed to Kalman filtering) is that the state is solved for at one particular time using a set of observations, rather than at the time of each observation. The initial time t_0 for which the solution is generated is known as the batch epoch. If the state vector is defined as the $n \times 1$ vector containing the parameters to be estimated, then the dynamic equations governing the problem can be described by a system of differential equations:

$$\dot{\boldsymbol{X}}(t) = F(\boldsymbol{X}(t), t) \tag{B.1}$$

In the case of gravity field recovery, these differential equations are nonlinear. The nominal trajectory represents the calculated value of the state vector according to pre-determined models. The nominal values are denoted with an asterisk, so that the corresponding nominal dynamic equations become

$$\dot{\boldsymbol{X}}^*(t) = F(\boldsymbol{X}^*(t), t) \tag{B.2}$$

Naturally, the computed nominal trajectory will not be a perfect representation of the true state, so the $n \times 1$ deviation vector between the two is introduced:

$$\boldsymbol{x}(t) \equiv \boldsymbol{X}(t) - \boldsymbol{X}^*(t) \tag{B.3}$$

The time derivative of the deviation is desired in order to form a differential equation describing the relative behavior between the two trajectories:

$$\dot{\boldsymbol{x}}(t) = \dot{\boldsymbol{X}}(t) - \dot{\boldsymbol{X}}^*(t) \tag{B.4}$$

Recall that the derivative of the true state $\dot{\boldsymbol{X}}(t)$ is a set of nonlinear differential equations. To simplify the problem, these equations are linearized about the derivative of the nominal trajectory via a Taylor series expansion. The Taylor series approximation is valid as long as the nominal trajectory is sufficiently close to the true trajectory.

$$\begin{aligned}\dot{\boldsymbol{x}}(t) &= F(\boldsymbol{X}(t),t) - F(\boldsymbol{X}^*(t),t)\\ &= F(\boldsymbol{X}^*(t)+\boldsymbol{x}(t),t) - F(\boldsymbol{X}^*(t),t)\\ &= \left\{F(\boldsymbol{X}^*(t),t) + \left[\frac{\partial F(\boldsymbol{X}(t),t)}{\partial \boldsymbol{X}}\right]^* \boldsymbol{x}(t) + h.o.t.\right\} - F(\boldsymbol{X}^*(t),t) \end{aligned} \tag{B.5}$$

The higher order terms can be ignored if the deviation is small, so the variational equations can now be established:

$$\dot{\boldsymbol{x}}(t) = \boldsymbol{A}(t)\boldsymbol{x}(t) \tag{B.6}$$

where $\boldsymbol{A}(t)$ is an $n \times n$ matrix defined as

$$\boldsymbol{A}(t) = \left[\frac{\partial F(\boldsymbol{X}(t), t)}{\partial \boldsymbol{X}}\right]^* \tag{B.7}$$

The matrix $\boldsymbol{A}(t)$ can easily be calculated and so can $\boldsymbol{x}(t)$ by integrating Equation B.6, but the value of $\boldsymbol{x}_0$ (the deviation at the batch epoch) is ultimately desired. The State Transition Matrix $\boldsymbol{\Phi}(t, t_0)$ is used to map the deviations at different times to the batch epoch:

$$\boldsymbol{x}(t) = \boldsymbol{\Phi}(t, t_0)\boldsymbol{x}_0 \tag{B.8}$$

where $\boldsymbol{\Phi}(t_0, t_0) = \boldsymbol{I}$. The value of $\boldsymbol{\Phi}(t, t_0)$ can be obtained at any time by numerically integrating the equation

$$\dot{\boldsymbol{\Phi}}(t, t_0) = \boldsymbol{A}(t)\boldsymbol{\Phi}(t, t_0) \tag{B.9}$$

The observations of the satellite are incorporated into the estimation problem through the observation-state relation:

$$\boldsymbol{Y}(t) = G(\boldsymbol{X}(t), t) + \boldsymbol{\epsilon}(t) \tag{B.10}$$

where $\boldsymbol{Y}(t)$ is a $m \times 1$ vector containing the set of m observations taken during the data arc. The $m \times 1$ vectors $G(\boldsymbol{X}(t), t)$ and $\boldsymbol{\epsilon}(t)$ are the observation model that represents the mathematical model of satellite observations and observation error that accounts for the various reasons why an observation would be faulty, respectively. In a similar fashion to the dynamic equations, a nominal value of $\boldsymbol{Y}(t)$ can also be established. It contains the expected value according to the observation model when it is evaluated on the nominal trajectory:

$$\boldsymbol{Y}^*(t) = G(\boldsymbol{X}^*(t), t) \tag{B.11}$$

Deviations between the observation-state equation and the nominal observation equation will exist as well, taking the form:

$$\boldsymbol{y}(t) \equiv \boldsymbol{Y}(t) - \boldsymbol{Y}^*(t) \tag{B.12}$$

The $m \times 1$ vector of deviations is also sometimes referred to as residuals. A linearization via Taylor series expansion can be performed on $G(\boldsymbol{X}(t), t)$ to reach an alternate expression for the residual equation:

$$\begin{aligned} \boldsymbol{y}(t) &= G(\boldsymbol{X}(t), t) + \boldsymbol{\epsilon}(t) - G(\boldsymbol{X}^*(t), t) \\ &= G(\boldsymbol{X}^*(t) + \boldsymbol{x}(t), t) - G(\boldsymbol{X}^*(t), t) + \boldsymbol{\epsilon}(t) \\ &= \left\{ G(\boldsymbol{X}^*(t), t) + \left[\frac{\partial G(\boldsymbol{X}(t), t)}{\partial \boldsymbol{X}} \right]^* \boldsymbol{x}(t) + h.o.t. \right\} - G(\boldsymbol{X}^*(t), t) + \boldsymbol{\epsilon}(t) \end{aligned} \tag{B.13}$$

Again, the higher order terms resulting from the Taylor series expansion can be neglected without much loss of accuracy if the nominal and true trajectories are sufficiently close to each other. The vector $\boldsymbol{\epsilon}(t)$ now contains additional errors due to the truncation of the higher order terms. The final expression for the vector of residuals is:

$$y(t) = \tilde{\boldsymbol{H}}(t)\boldsymbol{x}(t) + \epsilon(t) \tag{B.14}$$

where $y(t)$ and $\epsilon(t)$ are scalar values corresponding to each individual observation. The deviation in the state, $\boldsymbol{x}(t)$, is $n \times 1$ and $\tilde{\boldsymbol{H}}(t)$ is $1 \times n$ and defined as:

$$\tilde{\boldsymbol{H}}(t) = \left[\frac{\partial G(\boldsymbol{X}(t), t)}{\partial \boldsymbol{X}}\right]^{*} \tag{B.15}$$

For the ith observation, the corresponding residual now takes the form:

$$y_i = \tilde{\boldsymbol{H}}_i\boldsymbol{x}_i + \epsilon_i \tag{B.16}$$

The State Transition Matrix can be employed again to map the observation taken at time t_i to the epoch time t_0. Introducing the $1 \times n$ information matrix as $\boldsymbol{H} = \tilde{\boldsymbol{H}}_i\boldsymbol{\Phi}(t_i, t_0)$ leads to

$$y_i = \boldsymbol{H}_i\boldsymbol{x}_0 + \epsilon_i \tag{B.17}$$

The set of individual observation residuals can be accumulated as such

$$\begin{bmatrix} y_1 \\ y_2 \\ \vdots \\ y_m \end{bmatrix} = \begin{bmatrix} \boldsymbol{H}(t_1) \\ \boldsymbol{H}(t_2) \\ \vdots \\ \boldsymbol{H}(t_m) \end{bmatrix} \boldsymbol{x}_0 + \begin{bmatrix} \epsilon(t_1) \\ \epsilon(t_2) \\ \vdots \\ \epsilon(t_m) \end{bmatrix} \tag{B.18}$$

and can be simplified into the following equation

$$\boldsymbol{y} = \boldsymbol{H}\boldsymbol{x}_0 + \boldsymbol{\epsilon} \tag{B.19}$$

The dimension of $\boldsymbol{y}$ is $m \times 1$ and $\boldsymbol{H}$ is $m \times n$. Furthermore, $\boldsymbol{x}_0$ is $n \times 1$ and $\boldsymbol{\epsilon}$ is $m \times 1$. This equation is solved using weighted least squares. To do this, the normal equations are formed or an orthogonal factorization (discussed in a future section) is performed on $\boldsymbol{H}$ to obtain the best estimate of the deviation between the nominal and true trajectories [8]. The normal equations arise from the notion that the weighted least squares solution is obtained via the minimization of the square of the observation residuals. This is characterized mathematically by introducing the performance index J:

$$J(x) = \boldsymbol{\epsilon}^T \boldsymbol{W} \boldsymbol{\epsilon} \tag{B.20}$$

where $\boldsymbol{W}$ is $m \times m$ and contains the weights assigned to each observation:

$$\boldsymbol{W} = \begin{bmatrix} w_1 & 0 & \dots & 0 \\ 0 & w_2 & \dots & 0 \\ \vdots & \vdots & \ddots & \vdots \\ 0 & 0 & \dots & w_m \end{bmatrix} \tag{B.21}$$

Equation B.19 can be rearranged to solve for $\boldsymbol{\epsilon}$ and inserted into the above equation to provide an alternate expression for the performance index:

$$J(x) = \left[\boldsymbol{y} - \boldsymbol{H}\boldsymbol{x}\right]^T \boldsymbol{W} \left[\boldsymbol{y} - \boldsymbol{H}\boldsymbol{x}\right] \tag{B.22}$$

Note that the notation has changed slightly in the above equation, but only for the purpose of simplification. The performance index is minimized by setting $\frac{\partial J}{\partial \boldsymbol{x}}$ equal to zero. This solution results in the normal equations.

$$\boldsymbol{H}^T\boldsymbol{W}\boldsymbol{H}\boldsymbol{x} = \boldsymbol{H}^T\boldsymbol{W}\boldsymbol{y} \tag{B.23}$$

Assuming the normal matrix $\boldsymbol{H}^T\boldsymbol{W}\boldsymbol{H}$ is invertible, the normal equations can be rearranged to provide the least squares solution for the deviation between the nominal and true trajectories:

$$\hat{\boldsymbol{x}}_0 = (\boldsymbol{H}^T\boldsymbol{W}\boldsymbol{H})^{-1}\boldsymbol{H}^T\boldsymbol{W}\boldsymbol{y} \tag{B.24}$$

This deviation can be used as an update the the nominal trajectory to obtain a new nominal trajectory:

$$\hat{\boldsymbol{X}}_0 = \boldsymbol{X}_0^* + \boldsymbol{x}_0 \tag{B.25}$$

The update is calculated using a linear assumption in the least squares formulation. However, the problem is nonlinear so the correction will not be a perfect one [26]. The process is then repeated in an iterative fashion to keep correcting the nominal fashion until it converges to a solution that is sufficiently close to the true trajectory.

The variance-covariance matrix (or simply the covariance matrix) contains information regarding the uncertainties associated with each of the estimated parameters. The square roots of its diagonal values, known as formal sigmas, can be used to assess the quality of each parameter's solution. The covariance matrix is defined as follows:

$$\boldsymbol{P} = E\left[(\hat{\boldsymbol{x}} - E\left[\hat{\boldsymbol{x}}\right])(\hat{\boldsymbol{x}} - E\left[\hat{\boldsymbol{x}}\right])^T\right] \tag{B.26}$$

where E is the expected value of argument inside the square brackets. The expected value of $\hat{\boldsymbol{x}}$ is $\boldsymbol{x}$, so

$$\begin{aligned} \boldsymbol{P} &= E\left[(\hat{\boldsymbol{x}} - \boldsymbol{x})(\hat{\boldsymbol{x}} - \boldsymbol{x})^T\right] \\ &= (\boldsymbol{H}^T\boldsymbol{W}\boldsymbol{H})^{-1}\boldsymbol{H}^T\boldsymbol{W}E\left[\boldsymbol{\epsilon}\boldsymbol{\epsilon}^T\right]\boldsymbol{W}\boldsymbol{H}(\boldsymbol{H}^T\boldsymbol{W}\boldsymbol{H})^{-1} \end{aligned} \tag{B.27}$$

When the weight matrix $\boldsymbol{W}$ is taken to be the inverse of the covariance associated with the observations ($\boldsymbol{W} = \left\{E\left[\epsilon\epsilon^T\right]\right\}^{-1}$, the conventional form of the covariance matrix is obtained:

$$\boldsymbol{P} = (\boldsymbol{H}^T\boldsymbol{W}\boldsymbol{H})^{-1} \tag{B.28}$$

Appendix C

GRACE Data Processing

C.1 Summary of Processing Scheme

The production of GRACE gravity solutions begins with two data sets that contain the GPS double-differenced observations and K-band range rate (KBR) observations over the course of one arc (usually chosen to be one day). The GPS data contains samples taken every 30 seconds and the KBR measurements are every 5 seconds [7]. This data is input to the Multi-Satellite Orbit Determination Program (MSODP), which incorporates the dynamic orbit determination approach [21]. MSODP numerically integrates the partial differential equations of motion using highly accurate models for the gravitational forces to create a nominal trajectory [24]. This allows for the differences between the actual KBR measurements and those that correspond to the nominal trajectory (known as the observation residuals) to be computed. The observation redisuals and the partials of the observations with respect to the estimated parameters are then passed from MSODP to the Advanced Equation Solver for Parallel Systems (AESoP).

AESoP is a piece of software designed to compute a linear least squares solution to an input data set using orthogonal transformations (QR factorization) [7]. As part of this process, AESoP converts the matrix of partials that are passed from MSODP into the upper triangular R matrix that is used in QR factorization to obtain an estimated solution. In addition, the covariance and correlation matrices associated with the resulting solution are generated.

While a data arc over which the orbits are numerically integrated is usually one day, AESoP will generally be used to accumulate many arcs into a span of one month, producing a gravity solution that reflects that span. These monthly gravity solutions are the primary product of the GRACE mission, and a comparison of each month's behavior helps to identify the time-variable aspects of the Earth's gravity field. Another possibility is to combine monthly fields to create a longer span (sometimes a year or more) to obtain a mean gravity field. A visual representation of the GRACE data flow is shown below [8]:

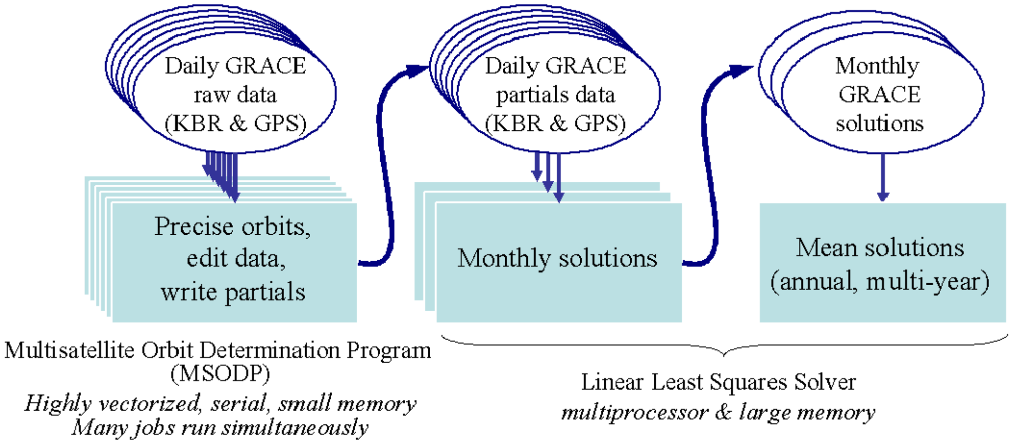

Figure C.1: Data flow during GRACE processing.

C.2 Estimated Parameters

The set of lumped harmonic coefficients that comprise a gravity solution are just a portion of the parameters being determined in the estimation process. The initial position and velocity of each satellite at the start of each arc are also solved for, as well as corrections to the double-differenced GPS measurements (ambiguity and zenith delay) [9]. The on-board accelerometer on each of the satellites experiences environmental influences on its signal, which have to be determined and nullified in the form of bias, rate, quadratic, and scale factor terms. Finally, the KBR measurements require corrections in a similar fashion, so low-low bias, rate, and periodic terms are also estimated. For a gravity field solution complete to degree and order 160, there will be around $26,000$ estimated parameters [8].

As mentioned previously, the data that gets incorporated into the gravity solution is made up of GPS and KBR observations. These measurements pertain to estimated parameters that are unique to their respective types, but there are also parameters that utilize both data sets for their solution. Also, some of the parameters are estimated over different time periods, such as the once-per-arc initial conditions and the monthly values of the harmonic coefficients. As a result, the ability to effectively distinguish between and organize these relationships is essential. To do this, GRACE processing incorporates a structure known as parameter leveling [8].

Parameter leveling is a way of classifying the different parameters according to their relationship with the observations, namely how much data and which type of measurement is used to determine the solution. The parameters are therefore grouped into three categories: local, common, and global. Local parameters are defined as those which only apply to one data arc (usually a day) and one type of data. Common parameters are valid for one arc as well, but contain data from both types of measurements. Finally, global parameters are those that pertain to all arcs and all data sets [22]. The classifications for each of the estimated parameter types for the latest version of GRACE releases (RL05) is listed below:

Table C.1: Default Parameter Classifications for GRACE

Local	Common	Global
Low-Low Bias	Initial Position	ACC Scale Factor
Low-Low Rate	Initial Velocity	Harmonic Coefficients
Low-Low Periodic	ACC Bias	
DD Ambiguity	ACC Rate	
DD Zenith Delay	ACC Quadratic	

With the parameter leveling scheme in place, the structure of the $\boldsymbol{H}$ matrix contains many zeros, which if included in the estimation routine would require many unnecessary operations. The adoption of QR factorization, which incorporates the upper triangular $\boldsymbol{R}$ matrix instead, is a useful way to eliminate many of these zeros.

If a hypothetical case involving 2 arcs and 2 data sets per arc is examined, the arrangement of values in $\boldsymbol{R}$ can be visualized. The local parameters, which contain information relating only to a specific arc and data type, are labeled L_{11}, L_{12}, L_{21}, and L_{22}. The first subscript denotes the arc number and the second one identifies the data set being used. The common parameters contain both data sets, but still have unique arcs and are called C_1 and C_2. Finally, the global parameters are represented by G. With this nomenclature established, the $\boldsymbol{R}$ matrix will look as follows [22]:

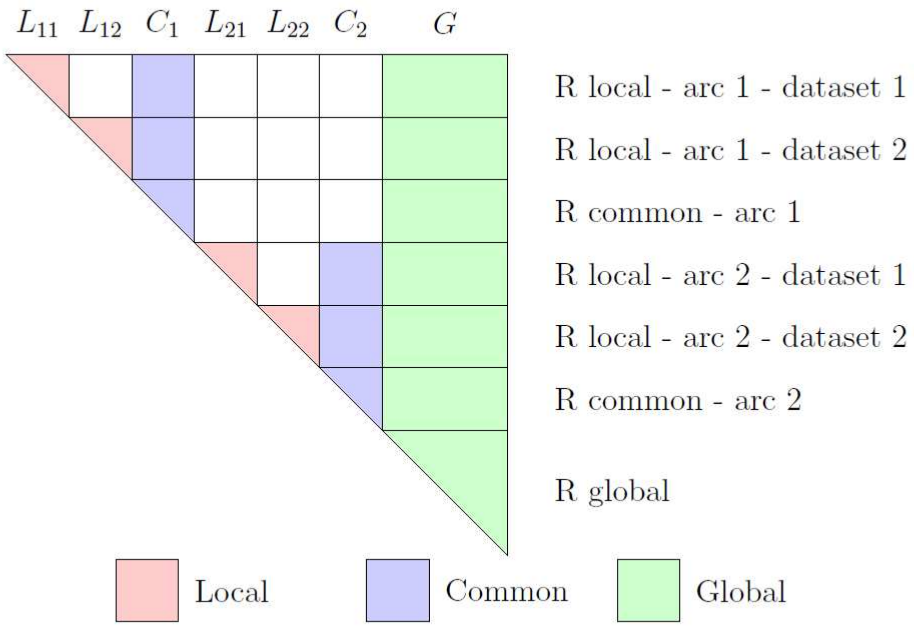

Figure C.2: Parameter leveling structure of the $\boldsymbol{R}$ matrix.

The white blocks in Figure C.2 correspond to locations in $\boldsymbol{R}$ that contain zeros. This representation of the information matrix requires far fewer unnecessary calculations than using the $\boldsymbol{H}$ matrix directly.

C.3 QR Factorization

As mentioned in Appendix B, the normal equations that result from batch processing are commonly solved for by inverting the normal matrix $\boldsymbol{H}^T\boldsymbol{W}\boldsymbol{H}$. However, the presence of an ill-conditioned problem can result in a loss of information if $\boldsymbol{H}$ contains values that are near machine precision [32]. Because of this, GRACE processing utilizes an orthogonal transformation technique known as QR factorization. By dealing directly with the $\boldsymbol{H}$ matrix, QR factorization is more accurate than inversion of the normal matrix during times of ill-conditioning [8]. The QR factorization method begins by introducing an orthogonal matrix $\boldsymbol{Q}$ that by definition does not affect the Euclidean norm of a vector when multiplied by it. The performance index introduced in Equation B.20 that is minimized to produce the least squares solution is re-written here for convenience:

$$J(x) = \boldsymbol{\epsilon}^T\boldsymbol{W}\boldsymbol{\epsilon} \tag{C.1}$$

The performance index can be rearranged to form the following:

$$\begin{aligned} J(x) &= [\boldsymbol{y} - \boldsymbol{H}\boldsymbol{x}]^T \boldsymbol{W}^{\frac{T}{2}}\boldsymbol{W}^{\frac{1}{2}} [\boldsymbol{y} - \boldsymbol{H}\boldsymbol{x}] \\ &= \left\{\boldsymbol{W}^{\frac{1}{2}} [\boldsymbol{y} - \boldsymbol{H}\boldsymbol{x}]\right\}^T \left\{\boldsymbol{W}^{\frac{1}{2}} [\boldsymbol{y} - \boldsymbol{H}\boldsymbol{x}]\right\} \\ &= \left|\left|\boldsymbol{W}^{\frac{1}{2}} [\boldsymbol{y} - \boldsymbol{H}\boldsymbol{x}]\right|\right|^2 \end{aligned} \tag{C.2}$$

The orthogonal matrix $\boldsymbol{Q}$ can be inserted into Equation C.2 without changing the magnitude of the performance index:

$$J(x) = \left|\left|\boldsymbol{Q}\boldsymbol{W}^{\frac{1}{2}}\left[\boldsymbol{y} - \boldsymbol{H}\boldsymbol{x}\right]\right|\right|^2 \tag{C.3}$$

The orthogonal matrix $\boldsymbol{Q}$ can be chosen such that

$$\boldsymbol{Q}\boldsymbol{W}^{\frac{1}{2}}\boldsymbol{H} = \begin{bmatrix} \boldsymbol{R} \\ \boldsymbol{0} \end{bmatrix} \tag{C.4}$$

where $\boldsymbol{R}$ is an $n \times n$ upper triangular matrix and $\boldsymbol{0}$ is an $(m-n) \times n$ null matrix. By selecting $\boldsymbol{Q}$ in this fashion, the following relationship is also established:

$$\boldsymbol{Q}\boldsymbol{W}^{\frac{1}{2}}\boldsymbol{y} = \begin{bmatrix} \boldsymbol{b} \\ \boldsymbol{e} \end{bmatrix} \tag{C.5}$$

where $\boldsymbol{b}$ is an $n \times 1$ vector and $\boldsymbol{e}$ is an $(m-n) \times 1$ vector. With these relationships in place, the performance index in Equation C.3 can be written:

$$J(x) = \left|\left|\begin{bmatrix} \boldsymbol{R} \\ \boldsymbol{0} \end{bmatrix}\boldsymbol{x} - \begin{bmatrix} \boldsymbol{b} \\ \boldsymbol{e} \end{bmatrix}\right|\right|^2 \tag{C.6}$$

This equation can be reduced to form the final expression for the performance index when utilizing QR factorization:

$$J(x) = ||\boldsymbol{R}\boldsymbol{x} - \boldsymbol{b}||^2 + ||\boldsymbol{e}||^2 \tag{C.7}$$

The quantity $||\boldsymbol{e}||^2$ is independent of the value of $\boldsymbol{x}$, so the solution that minimizes the performance index is simply:

$$\boldsymbol{R}\hat{\boldsymbol{x}} = \boldsymbol{b} \tag{C.8}$$

Since the $\boldsymbol{R}$ matrix is upper triangular, Equation C.8 is solved using simple back-substitution. Backwards substitution is computationally inexpensive when compared to performing a matrix inversion, an operation that is required in the conventional solution of the normal equations. However, when large amounts of data are involved, processing techniques that deal directly with the normal matrix will never invert it in the traditional sense. A more efficient alternative, such as a Cholesky decomposition, will be utilized instead. Accumulating the matrix and performing a Cholesky decomposition is less expensive than the QR Householder routine used in GRACE processing (n^2m versus $2n^2m$ FLOPs [20]), but the increase in accuracy when dealing with ill-conditioned problems justifies the increase in computation time.

The $\boldsymbol{R}$ vector contains information from both the $\boldsymbol{H}$ and $\boldsymbol{W}$ matrices in the original formulation. Therefore, tools such as the singular value decomposition can be used on $\boldsymbol{R}$ to infer the same results as if $\boldsymbol{H}$ were analyzed separately. Furthermore, this leads to a similar formulation for the covariance matrix as in Equation B.28 when Gaussian noise is assumed for the errors:

$$\boldsymbol{P} = (\boldsymbol{R}^T\boldsymbol{R})^{-1} \tag{C.9}$$

Bibliography

[1] S. V. Bettadpur. Orbital mechanics, perturbations, and grace science and mission design. Technical Report AAS 08-179, University of Texas Center for Space Research, Austin, TX 78759, 2008.

[2] S. V. Bettadpur. Gravity recovery and climate experiment level-2 gravity field product user handbook. Technical Report Rev 2.3, University of Texas Center for Space Research, Austin, TX 78759, February 20, 2007.

[3] J. Dongarra. *LAPACK User's Guide*. SIAM, third edition, 1999.

[4] G. H. Golub and C. F. Van Loan. *Matrix Computations*. The Johns Hopkins University Press, 1989.

[5] R. H. Gooding. Lumped fifteenth-order harmonics in the geopotential. *Nature Physical Science*, 231:168–169, 1971.

[6] Wagner C. A. Gruber C. Klokočník J. Kostelecký J. Gooding, R. H. Champ and grace resonances, and the gravity field of the earth. *Nature Physical Science*, 231:168–169, 2007.

[7] B. Gunter. *Computational Methods and Processing Strategies for Estimating Earth's Gravity Field*. PhD thesis, University of Texas-Austin, 2004.

[8] M. Hinga. *Using Parallel Computation to Apply the Singular Value Decomposition (SVD) in Solving for Large Earth Gravity Fields Based on Satellite Data.* PhD thesis, University of Texas-Austin, 2004.

[9] Nagel P. Pastor R. Kang, Z. Precise orbit determination for grace. *Adv. Space Res.*, 31(8):1875–1881, 2003.

[10] W. M. Kaula. *Theory of Satellite Geodesy.* Blaisdell Publishing Company, 1966.

[11] D. G. King-Hele. Lumped geopotential harmonics of order 14, from the orbit of 1967-11g. *Planet. Space Sci.*, 33(10):1145–1153, 1985.

[12] Walker D. M. C. King-Hele, D. G. Evaluation of 15th- and 30th-order geopotential harmonic coefficients from 26 resonant satellite orbits. *Planet. Space Sci.*, 37(7):805–823, 1989.

[13] Bezděk A. Kostelecký J. Sebera J. Klokočník, J. Orbit tuning of planetary orbiters for accuracy gain in gravity-field mapping. *Jour. of Guidance, Control, and Dynamics*, 33(3):853–861, 2010.

[14] Tapley B.D. Ries J.C. Poole S.R. Nerem, R.S. The joint gravity model 3. *Journal of Geophysical Research*, 1996.

[15] University of Texas Center for Space Research. Grace level-2 calibrated error repository. `ftp://podaac.jpl.nasa.gov/allData/grace/L2/CSR/RL04/`.

[16] Eckels A. Squires R. K. O'Keefe, J. A. Vanguard measurements give pear-shaped component of earth's figure. *Science, New Series*, 129(3348):565–566, 1959.

[17] Committee on Earth Gravity from Space. *Satellite Gravity and the Geosphere: Contributions to the Study of the Solid Earth and Its Fluid Envelopes.* National Academy Press, 1997.

[18] M. Pasupathy. A comparison of range and range-rate based grace gravity field solutions. Master's thesis, University of Texas-Austin, 2011.

[19] N. Pie. *Mission Design Concepts for Repeat Groundtrack Orbits and Application to the ICESat Mission.* PhD thesis, University of Texas-Austin, 2008.

[20] S. R. Poole. *Counting Operations.* Course notes.

[21] H.J. Rim and Bob E. Schutz. Geoscience laser altimeter systsem (glas) precise orbit determination (pod). Algortihm Theoretical Basis Document v 2.2, Center for Space Research, The University of Texas at Austin.

[22] H. Save. *Using Regularization for Error Reduction in GRACE Gravity Estimation.* PhD thesis, University of Texas-Austin, 2009.

[23] N. Sneeuw. *A Semi-Analytical Approach to Gravity Field Analysis.* PhD thesis, Technischen Universität München, 2000.

[24] Bettadpur S. Watkins M. Reigber Ch. Tapley, B.D. The gravity recovery and climate experiment: Mission overview and early results. *Geophysical Research Letters*, 31, 2004.

[25] Schutz B. E. Tapley, B. D. and G. H. Born. *Statistical Orbit Determination.* Elsevier, 2004.

[26] C. L. Thornton and J. S. Border. *Radiometric Tracking Techniques for Deep-Space Navigation.* Wiley-Interscience, 2003.

[27] D. A. Vallado. *Fundamentals of Astrodynamics and Applications.* Microcosm Press, 2007.

[28] Nerem R. S. Cefola P. Hagar H. Vetter, J. A historical survey of earth gravitational models used in astrodynamics from sputnik and transit to gps and topex. *AAS/AIAA Astrodynamics Specialist Conference*, AAS 93-620, Aug 16-19 1993.

[29] Schrama E.J.O Sneeuw N. Weigelt M. Visser, P.N.A.M. Dependency of resolvable gravitational spatial resolution on space-borne observation techniques. *Geodesy for Planet Earth*, 136:373–379, 2012.

[30] McAdoo D. Klokočník J. Kostelecký J. Wagner, C. Degradation of geopotential recovery from short repeat-cycle orbits: Application to grace monthly fields. *Jour. of Geodesy*, 80:94–103, 2006.

[31] J. M. Wahr. Time-variable gravity from satellites. Technical report, Cooperative Institute for Research in Environmental Sciences, University of Colorado, Boulder, CO 80309-0390.

[32] D. S. Watkins. *Fundamentals of Matrix Computations.* John Wiley and Sons, Inc., 1991.

Vita

Alex James Pini was born in Pittsburgh, Pennsylvania on 28 May 1988, the son of James M. Pini and Janice C. Pini and brother of Christine M. Pini. From 2002 to 2006, he attended Peters Township High School in McMurray, Pennsylvania. Upon graduation, he attended the Pennsylvania State University in 2006, where he majored in aerospace engineering. In 2010, he received the Bachelor of Science degree with Honors in Aerospace Engineering from the Pennsylvania State University. In the fall of 2010, he enrolled in the master's program for aerospace engineering at the University of Texas at Austin, focusing on the field of orbital mechanics. Throughout his time in graduate school, he worked as a graduate research assistant at the University of Texas Center for Space Research (CSR). He is set to start work as an aerospace engineer in late July, 2012 at ai solutions, Inc. in Lanham, Maryland.

Permanent address: ajp5095@gmail.com

This thesis was typeset with LaTeX[†] by the author.

[†] LaTeX is a document preparation system developed by Leslie Lamport as a special version of Donald Knuth's TeX Program.